Chimie Douce Approaches to Quantum Materials Synthesis

A Dissertation Presented for the

Doctor of Philosophy

Degree

The University of Tennessee, Knoxville

Nan Huang

May 2022

Copyright © 2022 by Nan Huang

All rights reserved.

ACKNOWLEDGEMENTS

Foremost, I would like to express my sincere gratitude to my principal advisor, Dr. David Mandrus, for his kindness, patience, and always being supportive of my academic study and research. When I struggled to make progress, he always pointed out the right direction and motivated me to innovate. He cherished every crazy idea I had and allowed me to give it a try. I want to thank Dr. Claudia Rawn for providing endless help and guidance to my research. My sincere thanks also go to Dr. Stephen Nagler, Dr. Jiaqiang Yan, Dr. Bryan Chakoumakos, and Dr. Weiwei Xie for helping me out when I was in a deep depression at my most challenging times. Thanks to Dr. Panchapakesan Ganesh and Dr. Kevin Roccapriore for helping me with the experiment in ORNL.

I would also like to thank all Dr. Mandrus's group members for helping and encouraging me during my most challenging times and creating a supportive educational environment.

I thank all my friends for all the fun we have had together.

Last but not the least, I would like to thank my family: my father Daxing Huang and my mother Chunmei Pan, for their generous love and support. I am incredibly grateful to my husband Hang Xiao for supporting me through my life's ups and downs and encouraging me to finish.

ABSTRACT

Over the past few decades, the forefront of materials physics has undergone a quiet revolution, ushering in the age of topological quantum materials. Earlier concepts holding that changes in a material's ground state were always intimately related to changes in symmetry have been expanded. It is now understood that there are "topological systems" where the state can be altered even though the symmetry remains unchanged. Among these systems, quantum spin liquids (QSLs) are of particular interest as paradigmatic examples which can be described in simple terms theoretically but exhibit strongly entangled quantum ground states and non-trivial topology. The hallmark of the QSL is the fractionalization of collective magnetic excitations that correspond to exotic particles such as Anyons or Majorana Fermions rather than the simple bosons (magnons) existing in conventional ordered magnets.

The research presented in this dissertation addresses the urgent need to find physical realizations of QSLs. In 2006 theorist A. Kitaev invented an exactly solvable model of a QSL based on a honeycomb lattice of S=1/2 spins connected by mutually incompatible Ising interactions[1]. In 2009, Jackeli and Khaliullin (JK) published a seminal paper that proposed a pathway to realize a Kitaev quantum spin liquid in a real material [2].

In the research presented here, we emphasize using chimie douce or "soft chemistry" approaches to the synthesis of new quantum materials, including intercalation, ion exchange, and hydrothermal techniques. Although these techniques are not new, it is only in the past few years that they have begun to have an appreciable impact on materials physics. The reason soft chemistry approaches are gaining ground is that they

offer an incredible synthetic richness compared to traditional thermodynamic approaches.

In this dissertation, we study some new honeycomb delafossite systems, $Ag_3LiM_2O_6$ ($M = Ru^{4+}$, Rh^{4+}, Ir^{4+}), in which the materials are synthesized using a gentle ion-exchange technique. We also study graphite that has been intercalated with $RuCl_3$. $RuCl_3$ is known to be "proximate" to a Kitaev QSL, and we hypothesized that by intercalating $RuCl_3$ into graphite, we could push $RuCl_3$ closer to an ideal Kitaev QSL.

TABLE OF CONTENTS

LIST OF TABLES

LIST OF FIGURES

CHAPTER 1. INTRODUCTION

Recently, due to the urgent demand for the development of quantum information storage, the investigation of topological quantum materials is one of the most popular fields in science. Topological material, just as its name implies, has the topological properties that can protect the information stored in the quantum state from degeneracy and in the meanwhile break the uncertainty principle of the qubit. Thus, the basic read operation will give us a specific result. These traits make the topological quantum material a good candidate for quantum computing. But how does it work? One of the practical models of this material can be described as follows: Imagine the spin of electrons is like a group dance as shown in Fig.1.1-1 from Ref. 3. For each electron, the way they are dancing is the same, that is, spin. But globally, for different states, the patterns are different. For example, in the spin-1/3 ground state, when two electrons move close to each other, one will step around them. Each time it travels $\pi/3$. Globally we have an unfamiliar dance pattern but locally, each electron just traverses its circle. This is called long-range entangle. This entanglement introduces a quasi-particle with 1/3 fractionalized electrons. When the spin is 5/2, which can be considered as 2+1/2, two whole electrons and ½ serve as the fractionalized quantum hall state [3]. The inter-reaction between the whole electron and spin-½ gives this system a more complicated state. That is Moore-Reed state. In this state, ½ electron is furtherly decomposed to a pair of conjugated quasi-particles, each of them carrying ¼ electron. Paired electrons always stay close to each other. The dancer must use four steps to go around this couple.

Therefore, in this system, we have symmetry from paired quasi-partials --- which give us degeneracy in an excited state as long as the distance between them is large enough.

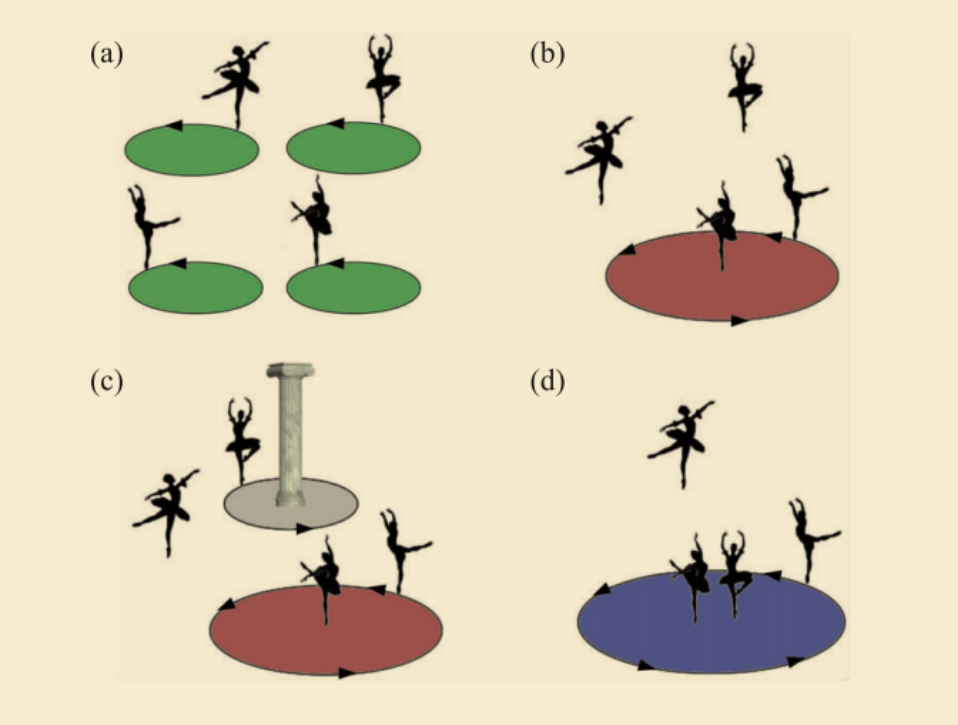

Figure 1.1-1 Scheme of group dance as an analog of Kitaev model. a) independent spin; b-c) spin-1/3 state d) spin-5/2 state; showing ½ spin decomposed to a pair of conjugated quasi-particles. Image is adopted from Ref. 3.

Since the Hamiltonian quantity in the system can be described as the sum of the local operator, the ground state is also degenerating. Meanwhile, the bandgap between the ground state and excited state protects the degeneracy.

1.1 Problem Statement

Moore's principle stated that the number of transistors on a single microchip would be doubled every two months [4]. However, constrained by the severe heat effect during data processing and transformation, classical computers' operating speed and efficiency are approaching their limit. The heat came from the information loss while utilizing conventional bit operation [5]. Besides, with the size of the transistor dangerously accessing the nanoscale, the classical physical properties are no longer applicable to explain its behavior. Instead, quantum physics takes the lead. In 1994, mathematician Dr. Shor proposed a novel algorithm to disintegrate large prime numbers using a quantum bit (qubit) to supersede the traditional bit [6]. The superiority of qubit is that each of its units can parallelly represent two different states which is twice as much as a regular bit. Hence, in an array of qubit, the amount of information it can carry is 2n times much more than that of a bit array (n is the size of the array). Consequently, it exponentially increases the storage and calculation speed.

However, the integration of qubit has faced great difficulties. If two states are close to each other, they will decoherent. Hence, we lose the information that is parallelly stored in qubit. One way to solve this problem is topological quantum computing [7], [8]. The qubit information is saved in the non-local parameter that has been protected by its topology. Global behavior will not be affected by the localized operation. One important candidate material that can achieve

these astonishing properties is quantum spin liquid material explained by Kitaev model [8]–[13]. In this model, they proposed a new particle, fractionalized electron, that has stable behavior globally. The interaction between electrons leads the movement. We will see the fractional quantum hall effect.

1.2 Original Contributions

In this research, we successfully synthesized two groups of new materials: new honeycomb delafossite systems $Ag_3LiM_2O_6$ ($M = Ru^{4+}$, Rh^{4+}, Ir^{4+}) and Metal chloride intercalated graphite

The contributions can be summarized as follows:

1. Synthesis of new honeycomb material as the candidate of spin liquid material. Achieved different compositions to compare and look for the correlation in this structure.

2. A detailed study of magnetic properties has been undertaken in $Ag_3LiM_2O_6$ to determine the nature of these new magnetic ground states. We solved the magnetic structure and atomic structure of this material using the neutron diffraction method. Fitted Warren-Equation on the stacking fault feature of these quasi 2D materials.

3. Successfully grown different halide intercalated graphite of bother poly and single crystal. Created a novel new method to encapsulate toxic halide gas into a sealed system. Prevent possible hazards pollution and danger. A modified synthesis method of $RuCl_3$ intercalated graphite.

4. A detailed study on the structure and properties of $RuCl_3$ intercalated graphite has been carried out.

Many common metal halides are known to intercalate graphite. Some of them have been intensely investigated on electronic properties such as $FeCl_3$ intercalated graphite [14]–[18]. Only one report showed that $RuCl_3$ could be intercalated into the graphite with many properties including electronic and magnetic behaviors remaining sealed. Besides, the number of stages of GIC material only indicated the stacking sequence along the c-axis. The detailed intraplane structure appears to be a challenging but significant task [19].

1.3 Organization of Document

Chapter 2 of this dissertation reviews background of two groups of new materials, delafossite and halide intercalated graphite, we selected for the project. It gives a detailed discussion of the current research on those two materials, pointing out the promising possibility of being a novel candidate spin liquid material stated in chapter 1.1 due to their two-dimensional honeycomb lattice and possible magnetic frustration. Chapter 3 discusses two methodology and experimental techniques we utilized in the project. Proposed advantages and potentials of this new method. Chapter 3 also introduces all the characterization techniques we used during the whole process. The following Chapter 4 demonstrates the results we discovered using the soft chemistry method on delafossite material $Ag_3LiM_2O_6$, Including the structural analysis and properties analysis. Chapter 5 demonstrates the progress we made on halide intercalated graphite and proposes three possible structures of stage-II sample based on diffraction data. The remaining document is references and the author's vita.

CHAPTER 2. LITERATURE REVIEW

2.1 Anyons and Kitaev Model

Anyons are particles with quantum statistics that neither Bose nor Fermi only existed in two-dimensional systems. Quantum statics is unusual statics that can be explained by a unique interaction: a pair particle-antiparticle interconvert along some specified trajectories. The overall quantum state of this particle pair system can be manipulated by a parameter $e^{i\varphi}$. Three-dimensionally, there is only one topologically distinct way to swap two particles. That is when and only when $e^{i\varphi} = \pm 1$. While in two dimensions, this parameter can be any value (that's why this kind of particle is called "Anyons", indicating that the global property will not be affected by the local change. This topological behavior keeps the information stored in a global pattern from the interference of local decoherence, thus making Anyons a good candidate for quantum information storage [20].

In 2005, Alexei Kitaev suggested that a topologically ordered state can serve as a physical analog of error-correcting quantum codes that can be applied in designing novel quantum memory [21]. Thus, the topologically ordered state can protect the information stored in qubits from decoherence. He proposed a fully solved model in a spin -1/2 system on a honeycomb lattice. Three different types of interactions, named "x-links", "y-links", and "z-links" are distinguished by their direction. The Hamiltonian term can be represented by the following equation [21] where J is the parameters:

$$H = -J_x \sum_{x-links} \sigma_j^x \sigma_k^x - J_y \sum_{y-links} \sigma_j^y \sigma_k^y - J_z \sum_{z-links} \sigma_j^z \sigma_k^z$$

These three types of interaction form swirling nanoscale spin vortices with Ising coupling that create an exchange frustration in each hexagon (Figure 2.1-1from Ref. 22). The ground state for S=1/2 moments on a 2D honeycomb lattice is an exactly solvable quantum spin liquid (QSL). Each Fractionalized spin excitations in the QSL are topologically protected gauge flux and Majorana fermion pairs [22]

2.2 Mott Insulator with Large Spin Orbital Coupling

The transition metal compound with partially filled d-levels has been under the spotlight and extensively studied after the recent discovery of multiple new phases and novel physical behaviors. Among them, the special phenomenon is that the spin orbitals in this system remained in a liquid state down to zero absolute temperature and showed strong quantum fluctuations. In other words, the spins kept a slow fluctuation and broke the long-range ordered state.

The material with mott phase transition (metal- Insulator transition) is called mott insulator. A classic example is the d^5 transition metal compound. Due to the relativistic small electron correlation energy, the material is expected to have metallic behavior. However, experimentally it exhibits an antiferromagnetic insulator ground state.

Dr. Jackeli et al. suggests that the abnormal phenomenon is caused by strongly enhanced instincts spin-orbital coupling for the late transition metal ion such ads Ru, Rh, Ir, Os [2]. The investigation of optical absorption on an Ir^{4+}- doped $SrTiO_3$ system suggested a relatively high value of spin-orbital coupling (~380 meV).

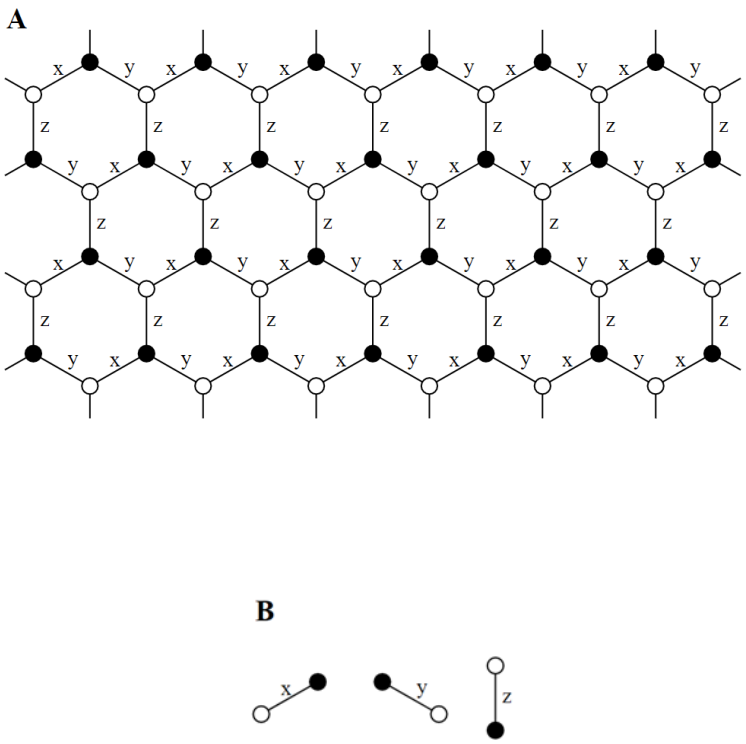

Figure 2.2-1 Three types of links in honeycomb lattice from Ref. 22.

This energy exceeds the intersite interactions, triggers the degeneration of t_{2g} orbit, and forms two child-level $J_{eff} = ½$ and $J_{eff} = 3/2$. It will result in the diminution of the energy band. Thus, even a relatively small correlation energy can create a bandgap [23].

There are two types of mott insulators with strong orbital coupling, as shown in Figures 2.2-1 from Ref. 2. The triangular lattice is correlated to ABO_3 (where B is the transition metal ion compound while the hexagonal lattice can be fitted with the Kitaev spin model as shown in Figure 2.2-1b. One example is the Li_2RuO_3. By replacing S = 1 ion Ru^{4+} with S = ½ Ir^{4+} ions, the resulting material Li_2IrO_3 may realize a strongly spin-orbital coupled Mott insulator with low energy physical behavior described by the Kitaev model [24].

2.3 Soft Chemistry Synthesis Method

Although an attempt of a panoply of different synthesis methods was undergoing in this project, soft chemistry is the one that we focused on, including ion exchange, intercalation, and hydrothermal techniques. Soft chemistry indicates a gentle chemical transformation of metastable structures from one to another. That is, gently regulating the composition, structure, phase, or interface while not severely disrupting original features. Thus, leading to relatively predictable properties of final products and a more practical design of new material. By minimizing the use of high temperature or other requirements of extreme conditions, soft chemistry, as an up-rising start in the synthesis of solid-state materials [25], [26], offers incredible synthetic richness compared to traditional thermodynamic approaches. Current existing soft chemistry techniques of particle formation enable different ways to control the size and crystallization of synthesized products as well as increase the crystal quality

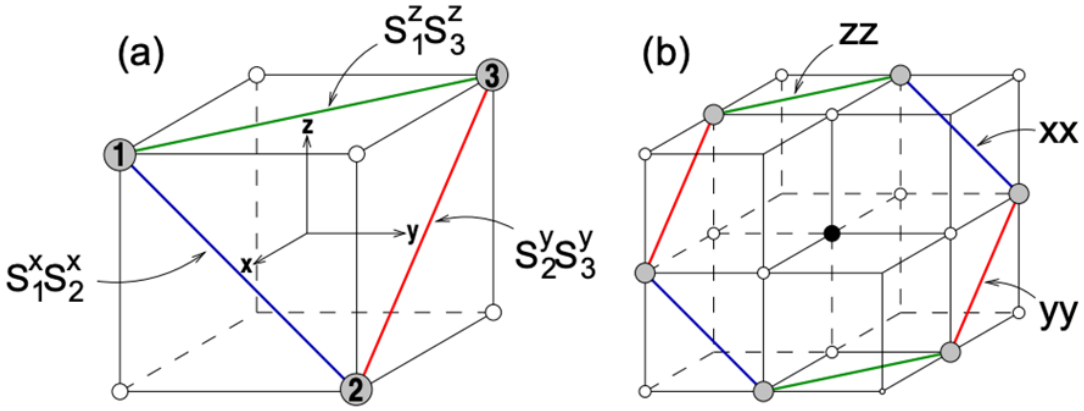

Figure 2.3-1(a) Triangular unit cell of ABO_2-type layered compounds, grey cycle represents magnetic transition metal ions. (b) The hexagonal unit cell of A_2BO_3-type layered compound, in which magnetic ions (B-sites) form a honeycomb lattice. A realization of the Kitaev model from Ref. 2.

2.4 New Honeycomb Compound $A_3LiM_2O_6$ (A = Ag, Cu; M = Ir, Rh, Ru)

In condensed matter physics, the quantum spin liquid (QSL) refers to a spin state where quantum fluctuations destroy long-range magnetic order and spins remain disordered at even low temperatures [22]. It has long been believed that the spin rotational symmetry is necessary for a QSL state to support fractional spinon excitation. Without this symmetry, the system will finally approach an ordered state. However, in 2006, Kitaev proposed an unusual, solvable model in which the strong spin-orbit coupling destroys the spin rotational symmetry and still maintains a QSL state [27], [28]. This paradox broke the previous verdict and thrust this model under the spotlight. The possible realization of the Kitaev model in A_2MO_3 (A = Li, Na and M = Ru, Rh, Ir） and $RuCl_3$ with a honeycomb structure has been thoroughly discussed recently [17-23]. While Kitaev-type interactions are believed to play an essential role in these systems, the presence of additional exchange interactions, including Heisenberg terms, leads to magnetically ordered ground states that are highly sensitive to both structural details and the A-site cation [27], [29].

Recently, new honeycomb delafossite systems $Ag_3LiM_2O_6$ (M = Ru^{4+}, Rh^{4+}, Ir^{4+}) have been formed using material [30]–[32]. Through an ion-exchange method, Li ions separating the $[M_2LiO_6]^{3-}$ honeycomb layers in Li_2MO_3 are replaced by Ag ions. The Resulting compounds exhibit higher structural symmetry while preserving the quasi-two-dimensional nature of the magnetic honeycomb layers and strong spin-orbit coupling [31]–[33]. As shown in the Figure. 2.4-1 from Ref. 32. Given their layered honeycomb lattices with 4d and 5d magnetic ions, the delafossites are excellent and largely unexplored candidates to host Kitaev interactions. Preliminary susceptibility curves reported in [31], as well as our measurements, indicate the

onset of long-range magnetic order at ~ 100 K in $Ag_3LiRh_2O_6$, a strikingly different behavior than that of the parent compound, which undergoes spin-glass-like freezing at T_f~ 6 K [34]. No detailed study of magnetic properties has been undertaken in $Ag_3LiM_2O_6$ to determine the nature of these new magnetic ground states. We proposed to solve the magnetic structure and atomic structure of this material using the neutron diffraction method.

2.5 α-$RuCl_3$ and Other Halides Intercalated Graphite

Graphite intercalated material (GIC) refers to inserting atoms, ions, or compounds into the crystal lattice of layered graphite [35]. By intercalating other kinds of guest species, new physical behaviors will be tuned, such as the spin-glass state observed in FeCl3 intercalated graphite [14], [16], [18], [35]–[39]. In this process, no chemical bond breaking is involved. Thus, graphite maintains its two-dimensional honeycomb lattice. Intercalated species are periodically distributed in a graphite matrix. Due to its lamellar structure, the GIC material can be separated into nanoscale thin films, which give rise to interesting properties and many possible applications. The number of stages represents the number of graphite layers between two adjacent intercalated layers. As shown in a simple sketch map Figure.2.5-1

The application of GIC material includes 1) use of battery materials and electrodes or fabrication of infrared polarizers due to the increased electrical conductivity [35]; 2) catalyzing organic reaction to promote the efficiency of the process [40]; 3) construction of heat shield utilizing high thermal conductivity; Recently, a large number of transition-metal halide intercalation compounds have been the subject of 2D magnetism investigation [14], [16], [38], [41], [42].

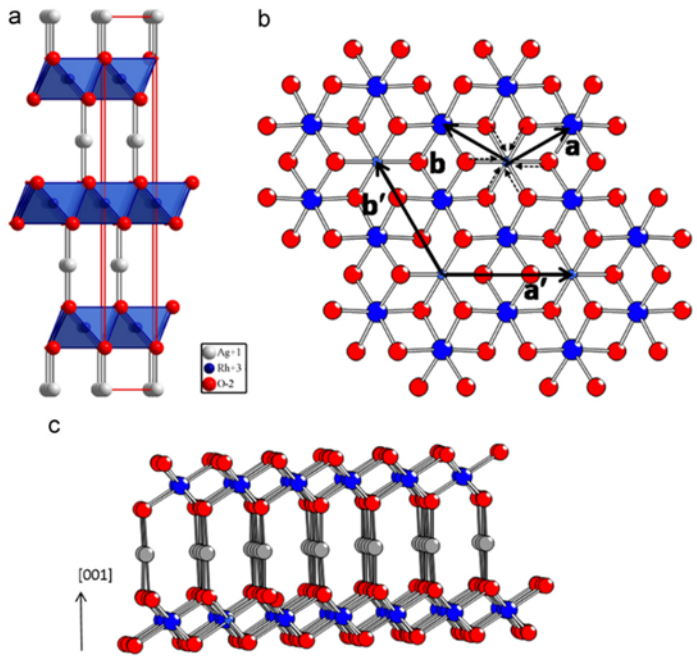

Figure 2.5-1 Delafossite structure ($R\bar{3}m$). With M = $Rh^{4+}$the dark blue part highlighting the RhO_6 octahedra. b) quasi-2D honeycomb lattice of $[M_2LiO_6]^{3-}$ cluster c) structure view along c-axis. The grey Ag atoms distributed between two layers of honeycomb structured octahedra. Image from Ref. 3.

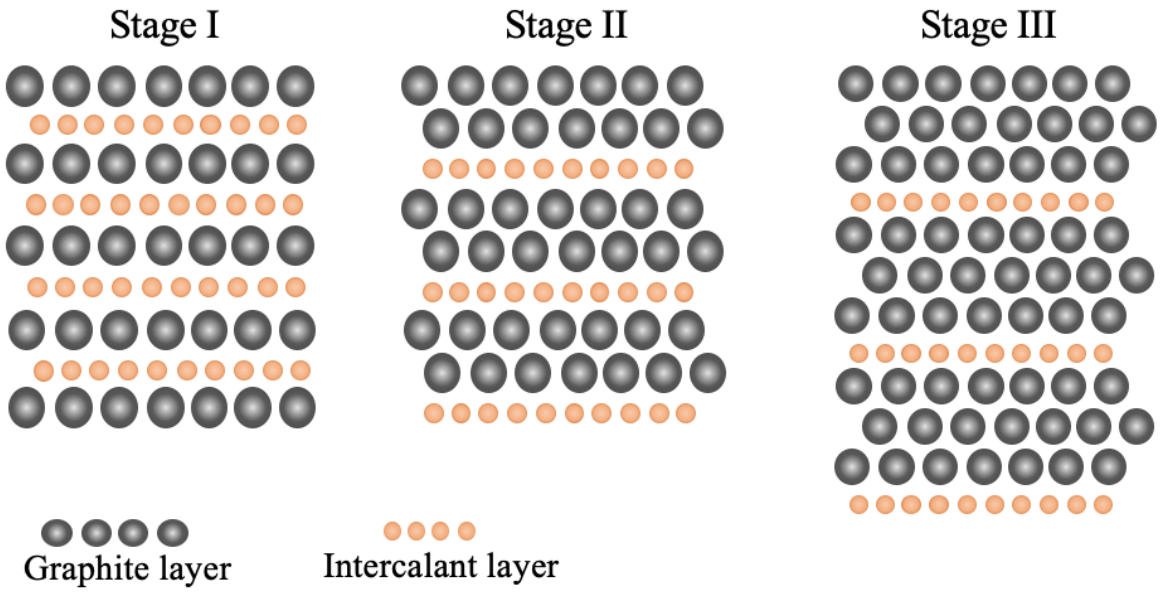

Figure 2.5-2 Abridged general view of graphite intercalated compounds of different stages.

More potential has been discovered in this kind of material. In our proposal, we are interested in the increased space between a-$RuCl_3$ layers that leads to a decreased interlayer coupling as well as a more two-dimensional magnetic behavior and hence gives rise to a potential candidate of Kitaev quantum spin liquid material. Moreover, considering $RuCl_3$ as either an insulator layer to form a metal-insulator-metal sandwich structure or a quantum fluctuating magnet layer between metallic graphite layer may possibly tune to interesting and surprising behavior, for example, superconductivity. Many common metal halides are known to intercalate graphite. Some of them have been deeply investigated in electronic properties, such as $FeCl_3$ intercalated graphite [14], [43]–[45]. Only one report showed that $RuCl_3$ could be intercalated into the graphite with many properties including electronic and magnetic behaviors remaining sealed. Besides, the number of stages of GIC material only indicated the stacking sequence along the c-axis. The detailed intraplane structure appears to be a challenging but significant task [19].

.

CHAPTER 3. METHODOLOGY

3.1 Sample Synthesis and Crystal Growth

3.1.1 Solid-State Reaction Synthesis Method

As a common synthesis technique, the solid-state reaction is widely utilized to produce polycrystalline oxides. The key idea of this method involves mixing and well-grinding of stoichiometrically weighed starting raw material, sintering in an open system under a relatively high temperature to simulate a chemical reaction through ion-diffusion in the melted oxide liquid. The new compounds of the designed composition are expected to harvest after being annealed under proper conditions, including starting reactants, atomic structure, particle size, Gibbs free energy, and thermodynamics involved in the reaction. Some factors can be tuned to produce the desired product [46]. For example, by changing the reaction atmosphere, we can adjust the oxidation state of one or multiple elements in the final product. Additional important factors include proper sample holder, pressure, and mixing homogeneities. In our project, the solid-state reaction method is employed to fabricate the parent material of delafossite honeycomb oxide. Li_2MO_3(M = Rh, Ru, Ir). Among them, Li_2IrO_3 and Li_2RuO_3 were simply synthesized by annealing stoichiometric and homogenous Li_2CO_3 and IrO_2/RuO_2 at 1273 K for 24 hrs, followed by another annealing at 1023K for 12hrs. Among them the only commercially accessible rhodium source of Li_2RhO_3 is Rh_2O_3, with a lower valence state compared to what we expect in the final product. The precursor Li_2RhO_3 was obtained by annealing stoichiometric amounts of Rh_2O_3 and Li_2CO_3 at 923 K for 12 hrs, followed by another heating cycle at 1223 K for 3 days under oxygen flow. Multiple regrinding and reannealing were carried out to ensure a homogeneous single phase in the final product.

3.1.2 Low-Temperature Ion-exchange Method

Compared to traditional solid-state reactions, as we discussed above, they share several factors, such as the reaction being motivated by ion-diffusion and the requirement of delicate grinding and mixing solid phase before sinter. The fundamental concept of these two methods is different. First, Ion-exchange utilizes appropriate salt with a relatively low melting temperature instead of oxide to serve as an 'exchanging ion' source which results in a much lower synthesis temperature. Second, ion exchange is a replacement reaction, while the solid-state is a synthetic reaction. Third, the ion-exchange reaction needs a closed vacuum system to prevent unnecessary oxidization and contamination from the ambient condition. This method can be considered as parent material dissolved in the molten salt. The free exchanging ion in the solution replaces the ion in the parent lattice, which has the same valence state. The ratio of replacement is constrained by 1) the size and activity of exchanging ions and 2) the atomic structure of the parent material [31]. As we can see in Figure 3.3-1 from Ref. 31, the honeycomb lattice, as well as the Li-Ru order in the honeycomb layer, are preserved after the ion-exchange process. Ag atoms only replace the interlayer Li atoms. In our project, $A_3LiM_2O_6$($A = Cu^+ Ag^+$, $M=Rh^{4+}$, Ir^{4+}) was synthesized by treating Li_2MO_3 in excess molten $AgNO_3$/CuCl. Li_2MO_3, $AgNO_3$/CuCl, and KNO_3/KCl with a molar ratio of 1:9:3 measured and mixed in the glovebox. The mixture was then pressed into the pellet and sealed in a sealed glass tube under a vacuum. The reaction was carried out in the muffle furnace at 573 K for around 7 days for an Ag-based sample and 673K for three days for a Cu-base sample. The residual nitride after the reaction was removed by washing reacted powder with deionized water five times, while the chloride needs to be washed off using diluted ammonia to remove excess Cu^+ ion. Then the powder was filtered out and dried at 373 K for 12 hours.

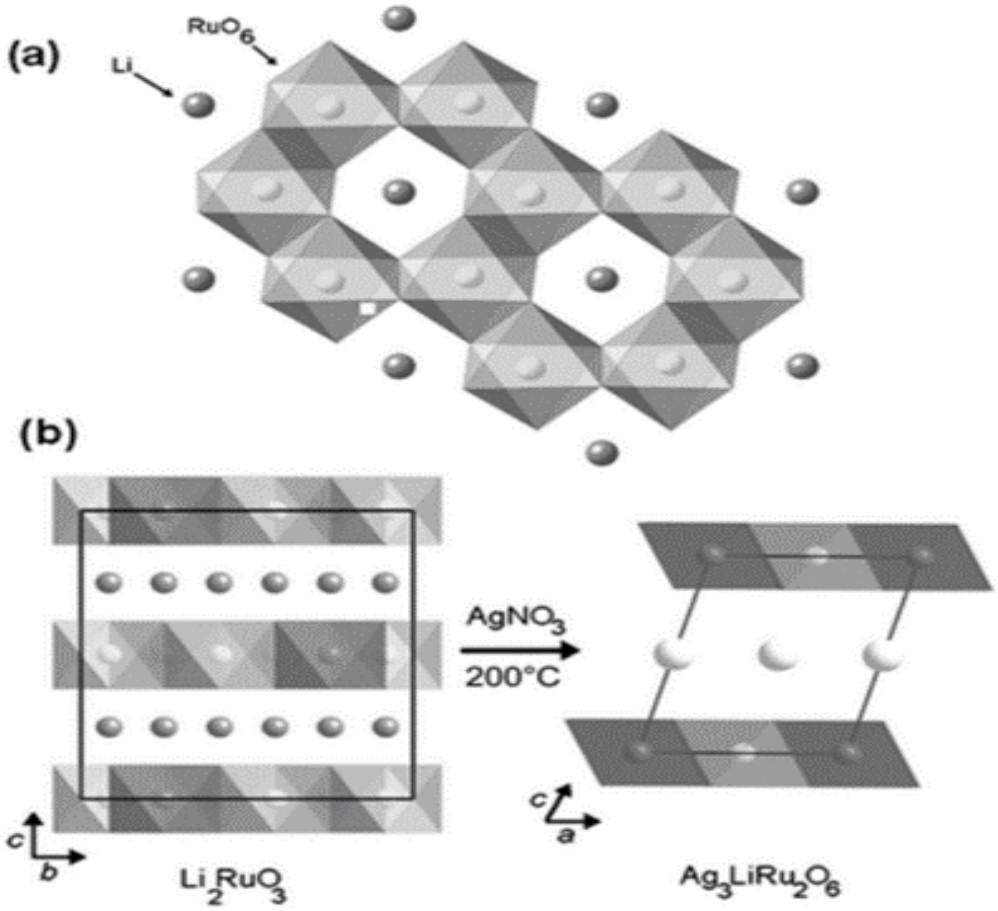

Figure 3.1-1 a) Honeycomb Li_2RuO_3 unit cell observed along c-axis. b) Ion-exchange synthesis of $Ag_3LiRu_2O_6$.

Image from Ref. 31.

3.1.3 Vapor Based Intercalation

Synthesis of graphite intercalates can be carried out using an intercalate in the vapor, liquid, or solid phase. Recently, researchers have designed and employed many novel or traditional synthesis techniques, including solid-state, molten salt, two-zone vapor transport intercalation and hydrothermal synthesis, etc., to fabricate graphite intercalating material [17], [42], [43], [47]. Among them, the two-zone vapor transport, as an intuitive, time-saving, fully developed method, is most widely used to intercalate volatile material into the graphite and obtain well-staged specimens [34,38-39].

Graphite and intercalant material is put in the different zone of a bulb tube with a neck in between, as shown in Figure.3.1-2. The intercalant is heated to a certain temperature T_i and vaporizes while the host graphite is heated to a higher temperature T_g to a) provide enough kinetic energy to trigger the intercalating reaction. b) to prevent the intercalant from depositing onto the surface of graphite. The difference between T_g and T_i can lead to a different stage of intercalation. From the viewpoint of chemical thermodynamics, the whole intercalation process can be divided into sfoursteps:1) The intercalant vaporizes and diffuse to the surface of graphite 2) The graphite absorbs the intercalant, and the intercalant is inserted from the edge of graphite. 3) The band forming 4) The stage transformation [44].

$$n\mathrm{C} + \mathrm{MCl_2}(s) + \frac{m}{2}\mathrm{Cl_2}(g) \rightleftarrows \mathrm{C}_n\mathrm{MCl}_{2+m}(s)$$

Therefore, the time-controlled steps are vaporization and insertion. The two-zone bulb tube can either be an open system to add the halide gas flow or a sealed, vacuumed system. The paper on C-RuCl3 published by V. A. Postnikov and A. V. Zvarykina has reported both ways that can successfully grow well-staged specimens[19]. However, after a long-term effort on

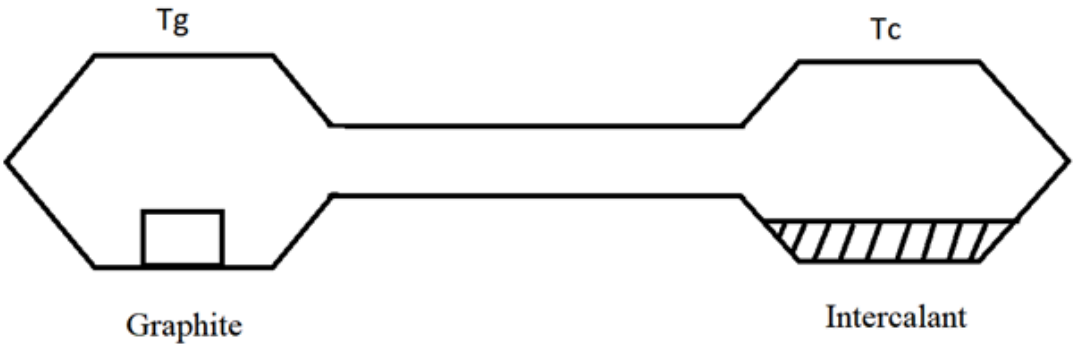

Figure 3.1-2 The scheme of two-zone vapor transport.

synthesis in a sealed vacuumed system, we confirmed that $RuCl_3$ is not able to be inserted into graphite lattice under this condition. The intercalation process can be represented by a reversible reaction as follows:

The chlorine atmosphere plays a significant role in pushing this reversible reaction to the right. Constrained by the lab safety rule of the university, we do not have access to a chlorine gas flow system. Thus, here we invent a novel, safe way to introduce hazarded halide gas in o a sealed system utilizing photosensitive material silver halide and a three-zone bulb tube.

As shown in Figure 3.1-3, additional to the hosted zone and intercalant zone, we introduce the chlorine source zone. The AgCl was ground into fine powder and transferred into a short silica tube which has a smaller diameter than the bulb tube. The three-zone bulb tube was then vacuumed and sealed. This process was carried out under a dimed light environment to prevent AgCl from decomposing. The chlorine source zone was treated under UV light till the color of the powder turned dark brown indicating the AgCl was fully decomposed into elemental silver and chlorine. The reaction is as follows:

$$2AgCl \xrightarrow{UV\ light} 2Ag + Cl_2 \uparrow$$

Finally, the source zone was removed to prevent Ag from recombination with Cl2 while annealing.

Through this process, we sealed only pure graphite(host), $RuCl_3$ powder (intercalant) and chlorine gas in a sealed system. By applying ideal gas function, we can estimate the pressure inside the tube while annealing.

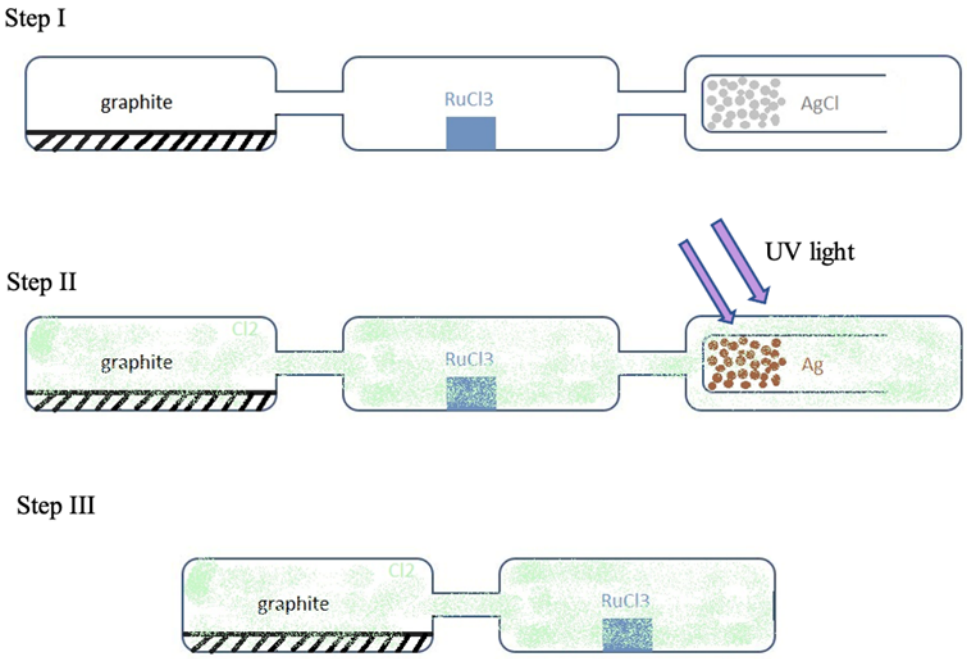

Figure 3.1-3 The scheme of two-zone vapor transport using AgCl as a chlorine source.

3.2 Characterization

3.2.1 X-Ray Diffraction

Powder X-ray diffraction is a characterization technique used for phase and purity identification of an unknown sample. In crystallography, this technique involves the interaction of incident X-rays with the atomic structure of a substance by scattering into various directions based on the material's structure. This results in unique diffraction peaks which are characteristic of the material's phase and structure, following Bragg's Law [48].

At the Joint Institute for Advanced Materials (JIAM), The crystal structure of the new honeycomb delafossite oxide and GIC sample was measured in a D8-Advance from Bruker AXS, equipped with a Ge (111)—Johansson monochromator, CuKα (λ=1.540598 Å). Refinements of each sample required the use of this data along with the General. A step of 0.02° was chosen and the data was collected in a 2θ range of 10° to 90°. Structure Analysis System II (GSAS-II) software was applied to determine the crystallographic parameters of the new Honeycomb compound $A_3LiM_2O_6$ (A = Ag, Cu; M = Ir, Rh, Ru) and intercalated graphite. However, the graphite we were using is mostly flake-like. We can still obtain the peaks from the 00l plane set and determine what stage it belongs to.

Single crystal X-ray diffraction will be utilized to determine the crystal structure of $RuCl_3$ intercalated graphite.

3.2.2 High-temperature X-ray Diffraction

Non-ambient X-ray diffraction is a useful tool for understanding a material's behavior in-situ with temperature change. In this proposal, high-temperature X-ray diffraction (HTXRD)

will be used to probe and deep investigate the kinetic and phase during metathesis reaction in the ion exchange.

3.2.3 High-pressure Synchrotron X-ray Diffraction

High-pressure synchrotron X-ray diffraction was developed in the late 1970s. It was the most widely used for in situ characterization of materials of their structure and properties. By combining the pressure vessel, for example, diamond anvil cells (DAC), with traditional synchrotron X-ray beamlines, this composite technique allows in situ measurement under high pressure. DAC is the most commonly used pressure vessel in this measurement. The functional pressure has a range of 0 – 400 GPa [49], [50], which can fulfill most characterization requirements. Another trait of the DAC cell is that the diamond is a material that is transparent to X-ray radiation due to its "minute size and optical absorption of diamonds in the beam path" with no background noise that needs to be eliminated afterward [51]. The single crystal C-$RuCl_3$ sample that was measured under an APS BL-13 model HP-SXRD in Dr. Bi Wenli's group under room temperature was synthesized through the novel three-zone vapor transport method. The sample was characterized under Bruker XRD machine using Cu-source with a wavelength of 1.54 Å to determine the stage as pure stage-II. The bulk sample was then cooled down to 77 K using liquid nitrogen to freeze the intercalated lattice and crushed into small pieces. Two small pieces of the sample were then transferred and loaded onto the DAC cell with a Daphne7575 pressure medium. The wavelength of HP-XRD was set at 0.4340 Å. The applied pressure ranges from 0.45 to 12.3 GPa.

Figure 3.2-1 from Ref. 49 shows the scheme of HP synchrotron X-ray diffraction.

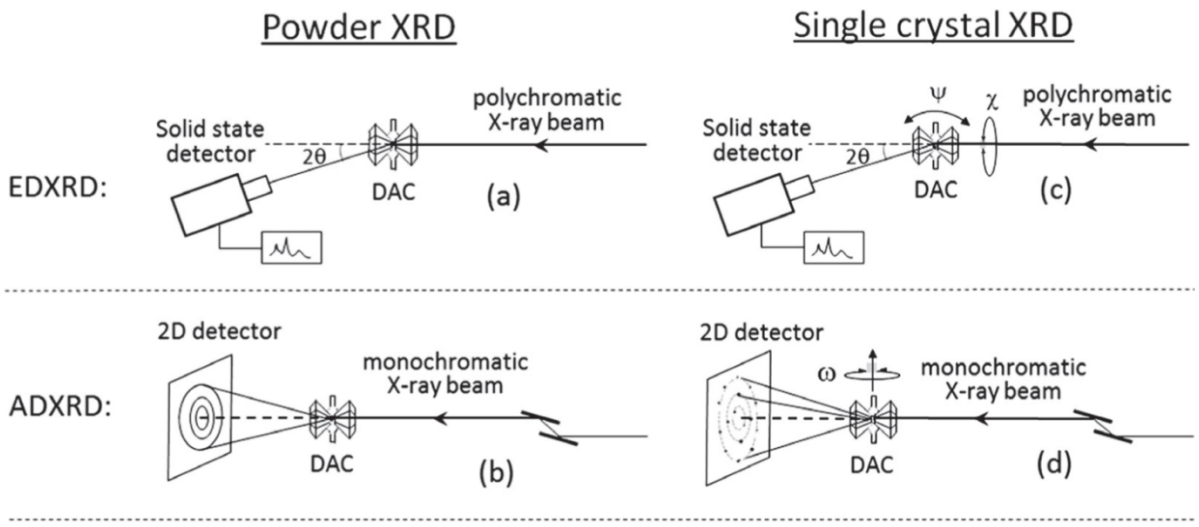

Figure 3.2-1 Scheme of high-pressure synchrotron X-ray diffraction. Image from Ref. 49.

3.2.4 Neutron Diffraction

Neutron diffraction data were collected using HB-1A and HB-2A powder diffractometer at the High Flux Isotope Reactor in Oak Ridge National Laboratory (ORNL). The experiment was carried out at temperatures 4 K and 50 K at HB-1A for both Ir and Rhsamplese. Rh sample was also measured in HB-2A at a temperature of 4 K and 120 K. The wavelength of incidence was $\lambda = 2.37$ Å.

3.2.5 Microscopy (SEM/EDX/STEM /STM)

Scanning electron microscopy and electron dispersive X-ray, also known as SEM/EDX, are techniques commonly used for the analysis and determination of a material's surface topography and element composition. It can review the surface of the sample by forming a distinct three-dimensional image. The working function is described as follows. The high-energy electron beam is accelerated by the beam gun and focused on the point of the sample. The electron in the atom of the skin layer receives this energy and is excited out of the sample. These dispersed free electrons are what we call secondary electrons. These secondary electrons carry the information on morphology. By scanning the sample point by point, an image displaying the topography of the surface is created. This process involves electrons from an electron beam interacting with the sample surface producing X-rays distinctive to the elements in the material. Sample purity, stoichiometric balance of the elements and composition homogeneity can be determined by this characterization technique. Accompany with the SEM image test. The EDS test also has been carried out to detect the element distribution on the surface. The high-energy E-beam generates not only secondary electrons but also other signals. For example, backscatter electron, transmitted electron, and characteristic X-rays. The EDS test is a technique that analyzes the

emitted X-rays when the inner shell electron transit to the outer shell to determine the certain atom it is from. Then map the distribution of the elements.

Microscopy of the sample surface was performed using a ZEISS EVO scanning electron microscope (SEM) with Bruker Flash 6130 energy dispersive X-ray spectrometer (EDXS) to prove the proper intercalation of $RuCl_3$ into the graphite.

3.2.6 Magnetic Properties (MPMS/SQUID)

Field-cool (FC) dc susceptibility was measured with a magnetic field of H=500 Oe in Superconducting Quantum Interference Device (SQUID) magnetometer. 10mg powder sample was loaded in a gelatin capsule and measured under a temperature range of 2 K to 300 K.

3.2.7 Electronic and Heat Capacity Measurement (PPMS)

Heat capacity was measured using a Quantum Design PPMS in the temperature range of 2 K to 200K. The powder sample was pressed into a pellet and cut into a proper cuboid shape with a size of 3mm*2mm*1mm using a diamond saw. The gold wire was connected to the sample by applying silver paint. The sample was then loaded onto the puck and transferred into the ppm.

CHAPTER 4. NEW HONEYCOMB MATERIALS $A_3LIM_2O_6$

4.1 Sample Preparation

In our project, $A_3LiM_2O_6$(A = Cu^+ Ag^+, M=Rh^{4+}, Ir^{4+}) was synthesized by treating Li_2MO_3 in excess molten $AgNO_3$/CuCl. Li_2MO_3, $AgNO_3$/CuCl, and KNO_3/KCl with a molar ratio of 1:9:3 measured and mixed in the glovebox. The powder needs to be grinder for more than 20 minutes to form a homogenous mixed powder. The sylvites are served as a fluxing medium to reduce the melting temperature of nitrides.

The mixture was then pressed into the pellet and loaded into a medium- sized quartz tube. After that, the tube was connected to a tube sealing station which has a vacuum system as well as the argon gas flow. The tube was first vacuumed than filled with argon. This washing process was repeated for three time to eliminate the influence of the residue air inside the tube. Finally, the tube was vacuumed using a turbo pump for 20 mins.

The reaction was carried out in the muffle furnace at ~573 K for around 7 days for an Ag-based sample and 673 K for 3 days for a Cu-base sample. The residual nitride after the reaction was removed by washing reacted powder with deionized water five times, while the chloride needs to be washed off using diluted ammonia to remove excess Cu^+ ion. Then the powder was filtered out and dried at 373 K for 12 hours. The chemical reactions are as shown below:

$$Li/Na_2MO_3+AgNO_3 \rightarrow Ag3Li/NaM_2O_6+ Li_2NO_3$$

$$Li/Na_2MO_3+CuCl \rightarrow Cu_3Li/NaM_2O_6+ 2LiCl$$

Table 4.1-1 List of New Honeycomb Structure Material Obtained.

$A_3LiM_2O_6$	Temperature ˚C	Time(days.)	Space Group
$Ag_3LiRu_2O_6$	300	5	*R-3m*
$Ag_3LiRh_2O_6$	270	7	*R-3m*
$Ag_3LiIr_2O_6$	270	7	*R-3m*
$Cu_3LiIr_2O_6$	400	3	*C12/c1*
$Cu_3NaIr_2O_6$	450	3	*C12/m1*

4.2 X-ray Diffraction

The atomic structure can be retrieved by refining both XRD and NPD data. The structure of $Ag_3LiRh_2O_6$ and $Ag_3LiIr_2O_6$ are very similar, as shown in Figure.4.2-1, 4.2-2. The only weak peak corresponding to a trace amount of Ag was exhibited on the pattern suggesting that the pure product was obtained. Both adopted a rhombohedral 3R-delafossite-type of structure. A corresponding structure, R-3m, was used in the refinement to interpret the basic atomic structure. The stacking fault can be observed as a Warren-shape line at a low angle (19.5°) with an index of non-integer indexes (1/3,1/3,0) which could not be explained using the 3R-delafossite structure model. The equation (1) and (2) was used to fit this Warren shape line [52].

$$P_{2\theta}{}' = KmF^2 \frac{(1+cos^2 2\theta)}{2(sin\theta)^{\frac{2}{3}}} \left(\frac{L}{\sqrt{\pi}\lambda}\right) W(a) \qquad (1)$$

$$W(a) = \int_0^{\infty} \exp\,(-x^2 - a)^2 dx \qquad (2)$$

where $a = \left(\frac{2\sqrt{\pi}L}{\lambda}\right)(sin\theta - sin\theta_0)$ The $P_{2\theta}{}'$ is called the power per absolute length of the circle that introduces the intensity of scattering per electron, K is a constant, L is the two-dimensional correlation length, and m is the two-dimensional multiplicity. F is also a constant of small ranges of angle. According to the equation above, we have the correlation length L calculated as 62.1nm and 380.1 nm for $Ag_3LiRh_2O_6$ and $Ag_3LiIr_2O_6$ respectively.

Correlation length L, which also refers to the length of periodic stacking fashion along the stacking direction. In this case, the random staking sequence is along the c axis.

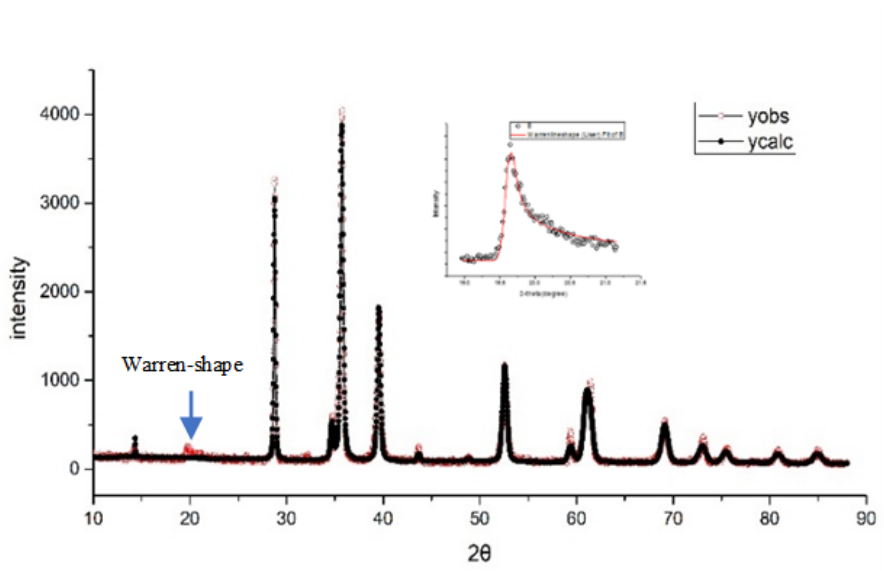

Figure 4.2-1 Powder XRD pattern of $Ag_3LiRh_2O_6$. In which the hollow circle is the experimental data while the filled circle represents the calculated data. The inset showed the zoom-in fitted Warren-shape line as pointed out by a blue arrow.

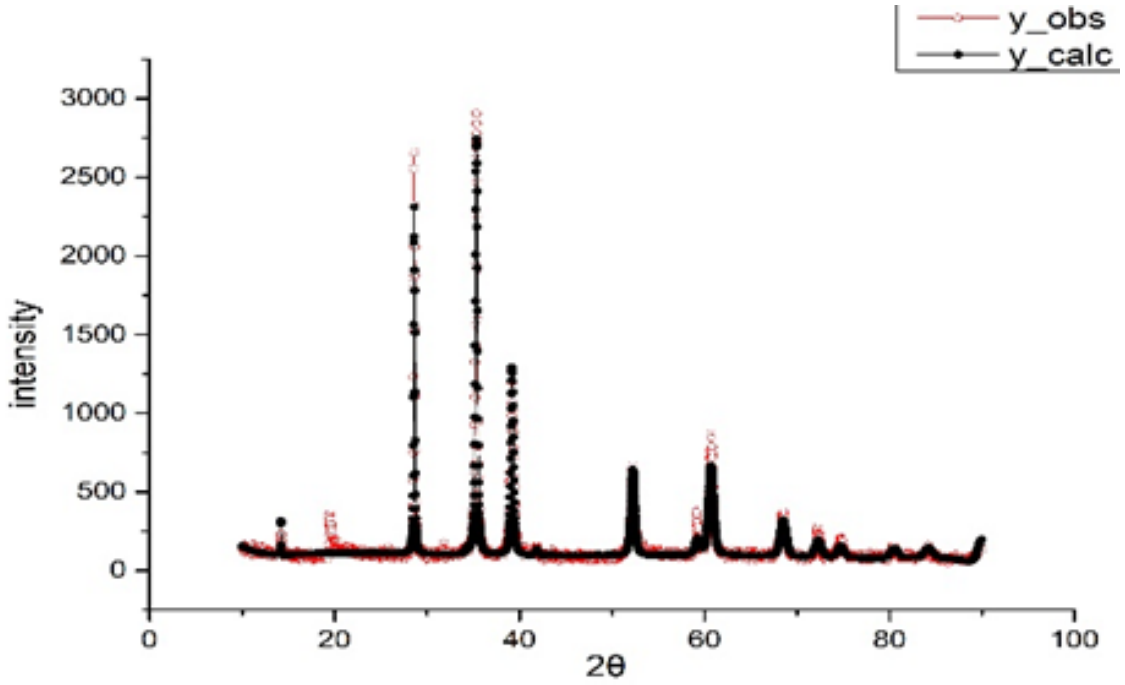

Figure 4.2-2 Refined Powder XRD pattern of $Ag_3LiIr_2O_6$ and fitted Warren-peak shape line.

As described by Todorova et al. [11], the circularly arranged sequence arises from the honeycomb layers $[M_2LiO_6]^{3-}$ stacking upon each other along with the c- axis while randomly shifting by any of the three directions s1=(a+b)/3, s2=−a/3 or s3=−b/3. In this case, the diffused scattering occurs at $\{hkl\}$ crystal plane where $h = (3n \pm 1)/3, k = (3m\pm)/3, l$,m, n are integers, and l is an arbitrary number. The two-dimensional reciprocal lattice can be considered as a series of layers parallel to each other. For each pair of h k, the smallest angle θ_0 should correspond to the 1/d value which is the minimum value distance of the diffused scattering line to the origin of the reciprocal space. With a random stacking sequence, this distance can be continuously distributed from the θ_0 to a certain boundary angle θ regarding a finite single-layer. At the boundary angle, the intensity contribution of that scattering line will drop to zero. Thus, an uninterrupted intensity distribution can be expected along with the full range from θ_0 to θ. A sawtooth shape for the intensity can also be explained by the fact that$|s_i - s_d|$changes slowly when the difference between θ_0 and θ. This theory will be furtherly discussed in the following STEM chapter.

4.3 STEM

The STEM was carried out to have an intuitive view of the layered structure of this kind of material. As we can see in Figure 4.3-1, The dark consequence white line on the image corresponds to a row of silver cations between two honeycomb layers of $[M_2LiO_6]^{3-}$. The dark line represents the edge-sharing Ir-Li octahedra. There is no obvious Ag vacancy in this material indicating a full replacement of Li between two honeycomb layers.

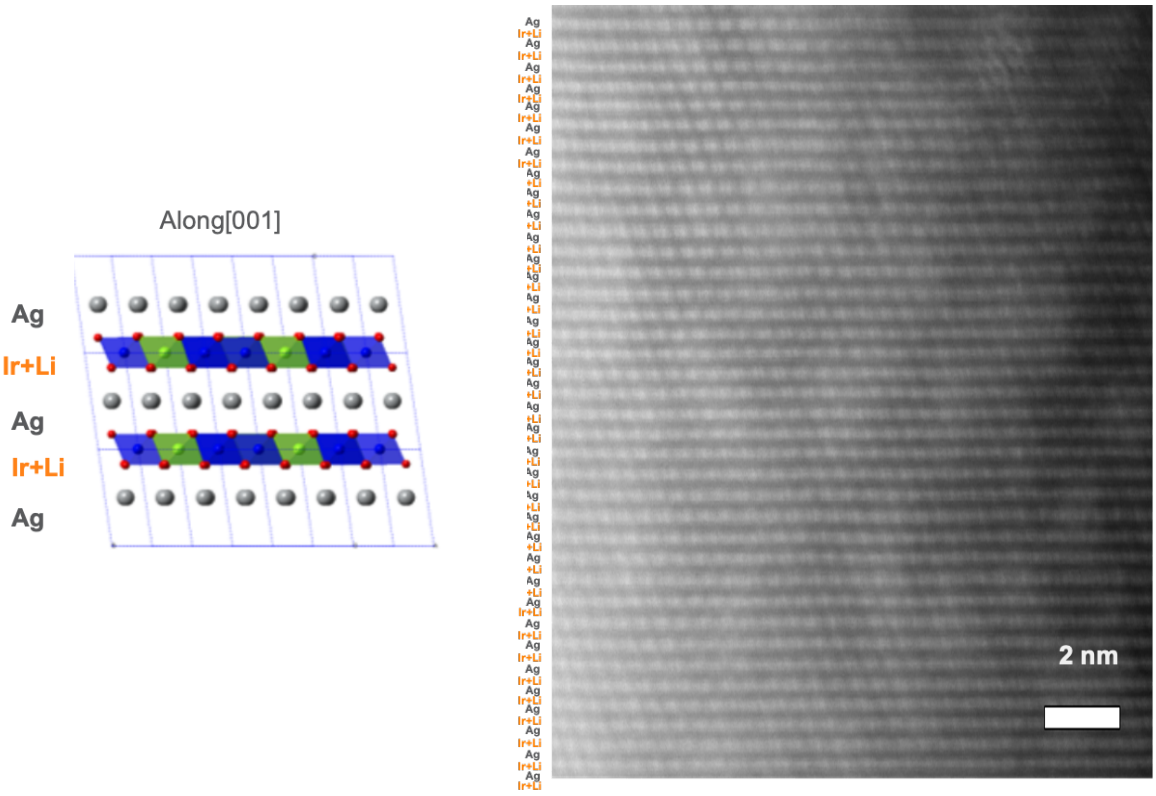

Figure 4.3-1 STEM image of $Ag_3LiIr_2O_6$ and the lattice structure along 00l direction.

4.4 HTXRD

HTXRD gives us a series of XRD patterns of the mixture while reacting. That helps us to understand how the chemical reaction works. As shown in Figure 94.4-1, Each line shape represents the peak we observed at a certain temperature. As we can see, at around 167°C, marked by an orange arrow, the characteristic peak of $Ag_3LiRu_2O_6$ appeared, marking the metathesis reaction starting. This is at the timestamp of two and half hours of heating. After four and half hours, all the precursor Li_2RuO_3 has been transformed into the final product. We refined every single XRD pattern we obtained during the heating process and listed the amount of each component in the reaction in percentage at the specified temperature.

From the Table 4.4-1, we can conclude that 1) the $AgNO_3$ started melting at 161 ˚C and melted at 173 ˚C. 2) The reaction starts as soon as $AgNO_3$ melts and it goes fast at the beginning temperature range (161-167 ˚C) and gradually slows down at higher temperature.

Figure 4.4-2 showed the weight ratio of three components versus temperature, the time interval between every neighboring two points of same color is 3 minutes. As we can see form the figure., there are several critical points on this figure: a) the $AgNO_3$ start melting at near 152 °C, the melting process finished in 15 minutes. At 162 °C, most of $AgNO_3$ has melted, the weight ratio of unreacted Li_2RuO_3 increased. The ion-exchange reaction stated. We can see the amount of $Ag_3LiRu_2O_6$ goes up. This metathesis reaction goes fast. It took only 12 mins to reach a considerable amount of $Ag_3LiRu_2O_6$. Then the amount of final product steadily increased in the following annealing.

We obtained substantial amount of final product at around 260 K.

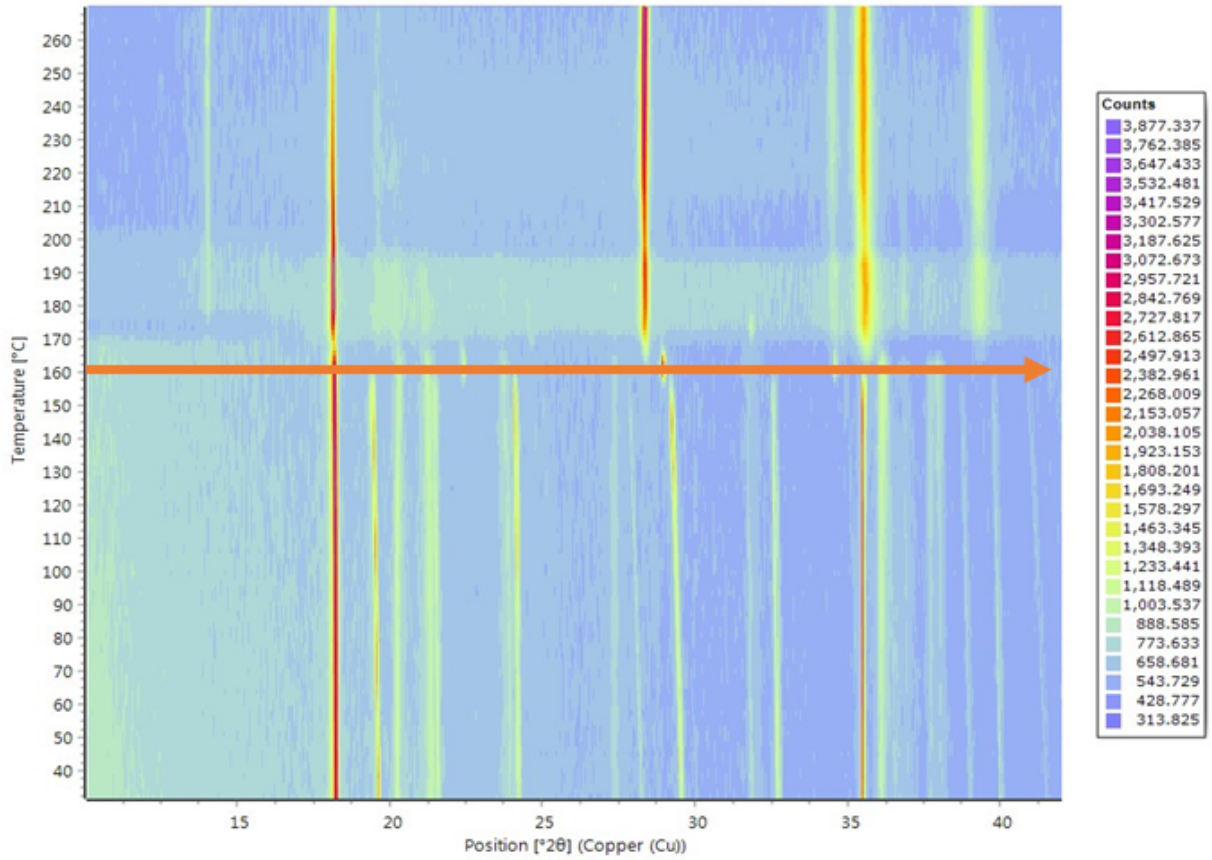

Figure 4.4-1 HTXRD color map of reaction $2Li_2RuO_3 + 3AgNO_3$ ---> $Ag_3LiRu_2O_6 + 3LiNO_3$.

Table 4.4-1 List of Amounts of Each Chemical Involved in the Metathesis Reaction.

Temperature ˚C	**$AgNO_3$**	**Li_2RuO_3**	**$Ag_3LiRu_2O_3$**
32	37.3%	62.7%	N/A
161	29.7%	66.8%	3.5%
167	9.3%	37.4%	53.3%
173	N/A	35.0%	65.0%
179	N/A	23.8%	76.2%
270	N/A	1.4%	98.6%

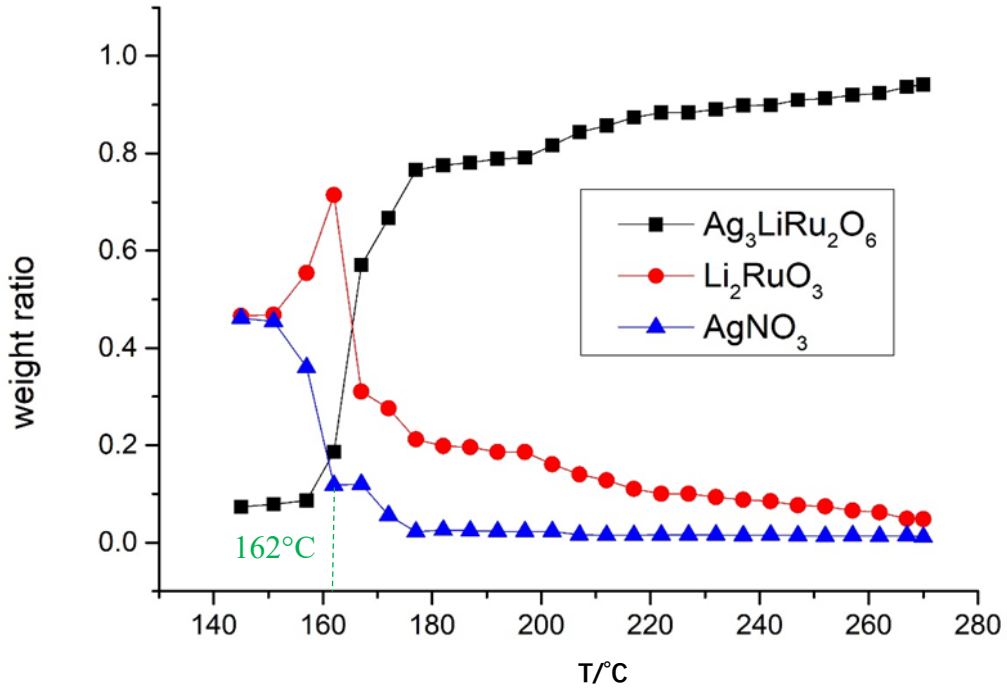

Figure 4.4-2 Wight ratios of each component versus T obtained from HTXRD data refinement.

4.5 Heat-capacity

Measuring the entropy fluctuation through heat capacity measurement is a shred of reliable evidence that indicates the presence of the possible phase transition. As shown in Figure.4.5-1a, an obvious turning point was observed at 92.17 K for the $Ag_3LiRh_2O_6$ sample which is close to the critical temperature obtained through magnetic susceptibility measurement. While for Ir-sample, it is hard to see the turning point on the Cp-T pattern, as shown in the Figure.4.5-1 b). Thus, we divided Cp of $Ag_3LiIr_2O_6$ by temperature T and obtained Cp/T-T data. The transition temperature Tc as labeled by the blue arrow, is around 12.14 K.

4.6 Magnetic Susceptibility

The magnetic property measurement was performed in a SQUID magnetometer. As seen in Figure 4.6-1, The sample $Ag_3LiRh_2O_6$ obeyed paramagnetic behavior in the temperature range of 150 K-300 K as well as obeying Curie-Weiss law and shows a cusp at 92.29 K consistent with an antiferromagnetic transition. The sample $Ag_3LiIr_2O_6$ also showed a paramagnetic behavior in the same temperature range with a transition temperature of 11.69 K.

By substituting the linear fitted line function (figure. 4-6.1 b) into the Curie-Weiss law $\chi=C/(T-\Theta_{cw})$. We obtain the Curie-Wiess constant as C_1 = 185.87 and C_2=1.05, Curie-Weiss temperature of 54.54 K and -168.28 K. The correlated effective magnetic moment was also calculated as μ_{eff}= 2.75. This effective magnetic moment does not agree with the spin-only value of 1.73 μ_B for the low-spin configurations of the $4d^5$ ion.

Those numbers match with the reference [23].

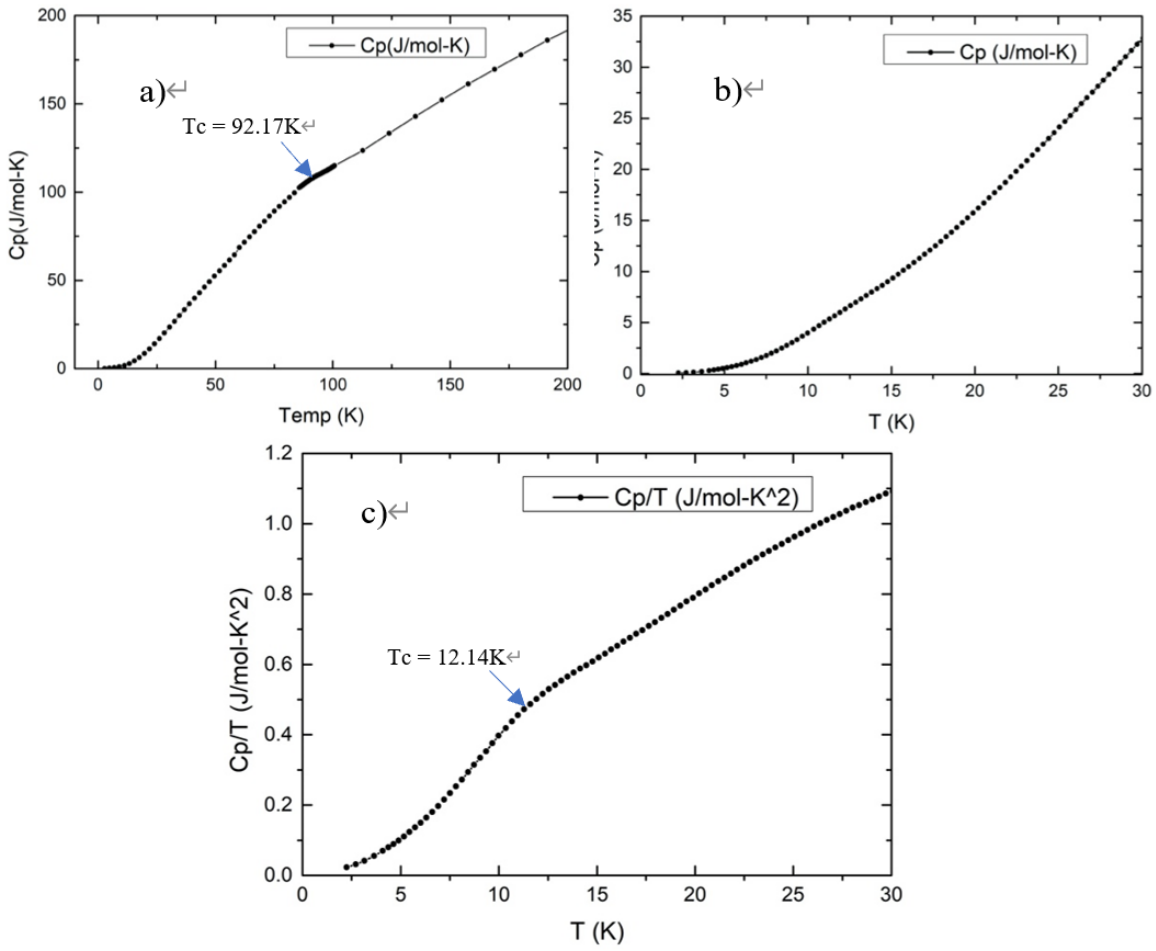

Figure 4.6-1 a) Heat-capacity of $Ag_3LiRh_2O_6$ measured from 2 K to 200 K. b) Heat-capacity of $Ag_3LiIr_2O_6$ Cp – T data. c） Cp/T – T data of $Ag_3LiIr_2O_6$.

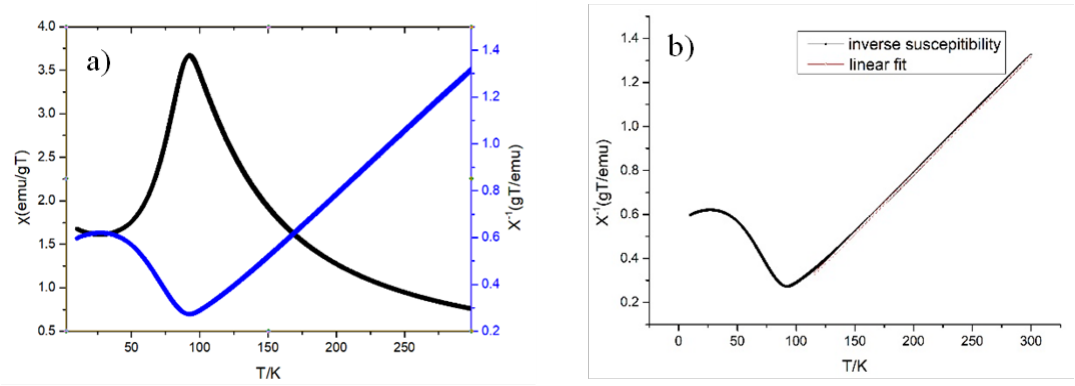

Figure 4.6-2 a) Magnetic susceptibility and inverse susceptibility plot of $Ag_3LiRh_2O_6$. b) Linear fit of inverse susceptibility of $Ag_3LiRh_2O_6$.

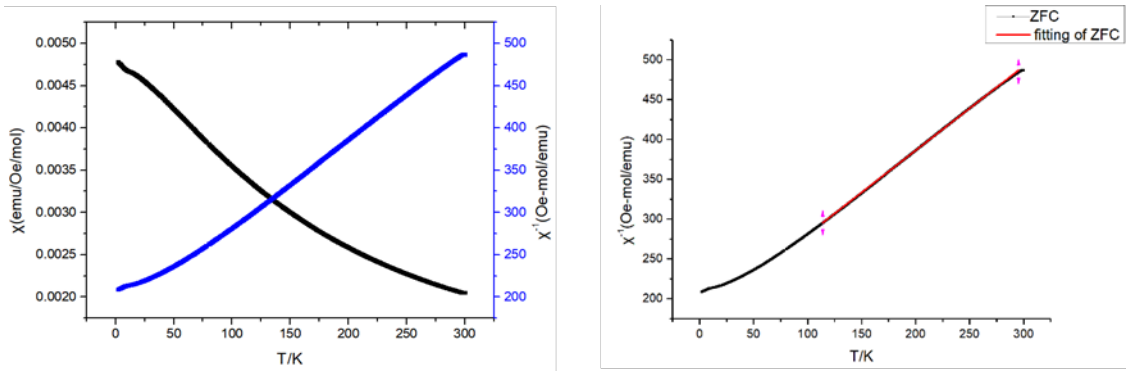

Figure 4.6-3 Magnetic susceptibilities and inverse susceptibility plot of $Ag_3LiIr_2O_6$ and linear fit of inverse susceptibility of $AgLiRh_2O_6$.

4.7 Neutron Diffraction and Magnetic Structure

The neutron data obtained in the HB1A neutron facility in the ORNL of this sample showed a clear magnetic peak at around 15.5°. By fitting with atomic rhombohedral structure and recursive analysis, we initially believe that this magnetic peak comes from the plane set (1/6, 1/6, 1/2), which is half of the Miller indices of Warren-shape peaks at 30.3°(1/3,1/3,1/2) that due to the random stacking fashion alone [00l] direction. The magnetic order in this material has a connection with the stacking fault. Regular diffraction shows that there is a part of the sample that has long-range crystalline order in only two dimensions. This produces a Warren line shape in the non-magnetic diffraction pattern, and perhaps the lack of long-range order in one direction is attributable to defects that we would call stacking faults. The scattering is consistent with that, but all we know is that it is quasi-2D. The magnetic Bragg peak signifies 3D magnetic order, but at a wavevector that shows, it originates from the part of the sample that produces the Warren line shape.

As discussed in magnetic susceptibility, the $Ag_3LiIr_2O_6$ sample is Antiferromagnetically ordered at low temperature. Of the three antiferromagnetic collinear spin arrangements, the Neel model will be rejected since it requires the similarity of the chemical unit cell and magnetic unit cell while we do not see an extra magnetic peak at low temperature as a conflict. Another possible model is Stripe. This model will result in a doubling on all three axes, which also does not match our observation. Thus, based on the feature that the magnetic unit cell doubled along the a and b axis, we suggest a magnetic model of Zig-zag to $Ag_3LiIr_2O_6$, which is introduced by stacking fault.

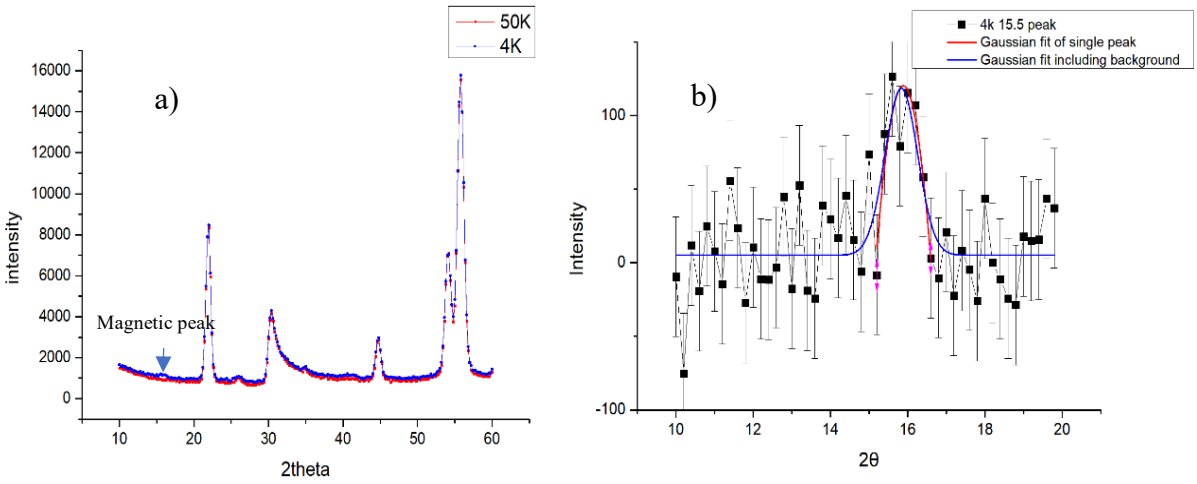

Figure 4.7-1 a) Neutron powder diffraction pattern of $Ag_3LiIr_2O_6$. b) Gaussian peak fit of the magnetic peak with error bar at 15.5°.

CHAPTER 5. METAL HALIDE INTERCALATED GRAPHITE

5.1 Sample Preparation

Several transition metal halide intercalated graphite was synthesized using different methods. The materials are listed in table 5.1-1:

Take the $FeCl_3$ as an example., the $FeCl_3$ intercalated graphite required extra $AlCl_3$ as a catalyst agent. The $FeCl_3$ and $AlCl_3$ powder was mixed and grinded in the glovebox and pressed into pellet. The pellet was transferred into the intercalant zone of a two-zone silica tube with graphite in the host zone and sealed under the vacuum. The tube was then sintered in a tube furnace with host zone (graphite) as hot end. Several rules that need to be considered while designing the experiment are listed as follows:

a) The choice of the sintering temperature was based on the boiling temperature of the intercalating chloride. Too high a temperature will introduce disorder into the lattice. b) Whether we need to use the three-zone method to introduce extra chlorine gas depends on the valance state of the intercalant. If the transition metal has a lower valance state than it exhibits in the intercalant. It will generate chlorine at high temperature upon decomposition. Otherwise, we must introduce extra chlorine to push the reversible reaction goes left. c) Longer annealing time will result in higher stage (more intercalation) sample.

High-quality Stage-II and Stage-IV C-$RuCl_3$ samples have been synthesized using three-zone method. Stage-II and IV indicate the number of graphite layers between two layers of $RuCl_3$. Figure.5.1-1 is a simple schematic diagram of the unit cell of two different samples.

Table 5.1-1 List of Synthesized GIC Material.

Sample	Synthesis method	stage	Temperature ˚C	Time (days.)
C-$FeCl_3$	Two-zone	2	350	5
		4		1
C-CuC_{l2}	Two-zone	1	430	14
		2		7
C-$MnCl_2$	Three-zone	4	550	5
C-$RuCl_3$	Three-zone	2	900	2
		4		22hrs

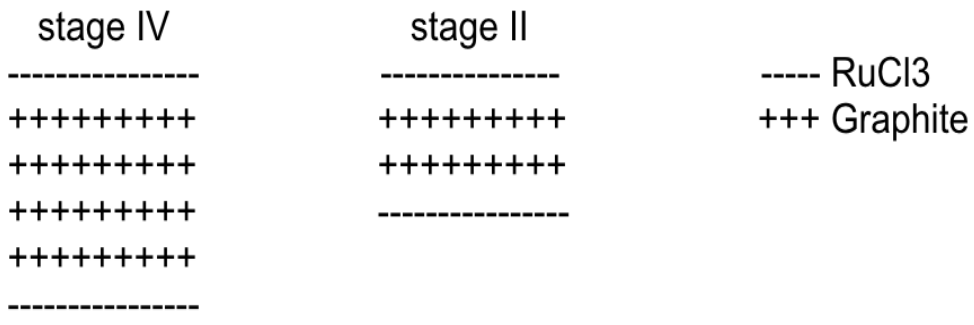

Figure 5.1-1 Sketch map of the unit cell structure of two different samples.

5.2 X-ray Diffraction and Analysis of C-$RuCl_3$ Sample

The XRD pattern (Figure. 5.2-1) showed pure stage-II and stage-IV single-crystal C-RuCl3 was obtained. Only 00L reflection can be seen on the pattern due to the preferred orientation. The intercalated graphite materials are sensitive to pressure (we will furtherly explain it in detail in the 5.6 high-pressure measurements). Grinding them into a fine powder and measuring them under the powder XRD machine to obtain other peaks from the ab-plane is not practical. A Clear left shift of the 00L peak compared to those on the original pure graphite pattern can be observed, which indicates a lattice expansion along the c-axis. Thus, the lattice parameter c of intercalated graphite should be larger than that of pure graphite (3.35 Å). Based on the position of each peak, we calculate the distance between two $RuCl_3$ layers by applying Bragg's law:

$$d_{00l} = \frac{n\lambda}{2\sin\theta}$$

d_{00l} of stage-II sample fitted from the position of the XRD peak is around 12.7 Å while stage-IV is close to 19.42 Å. Those numbers agreed with the original theoretical calculation.

With the lattice parameter c, we can calculate the distance between adjacent graphite and $RuCl_3$ layer, C-$RuCl_3$ distance can be calculated as lattice parameter c of stage-II unit cell minus the distance between two layers of graphite divided by two. This number can be cross-proved by substituting back into the stage-IV sample situation and calculating the lattice parameter c. We have calculated c equal to 19.41 Angstrom which is closed to what we obtained from the experimental XRD peak position.

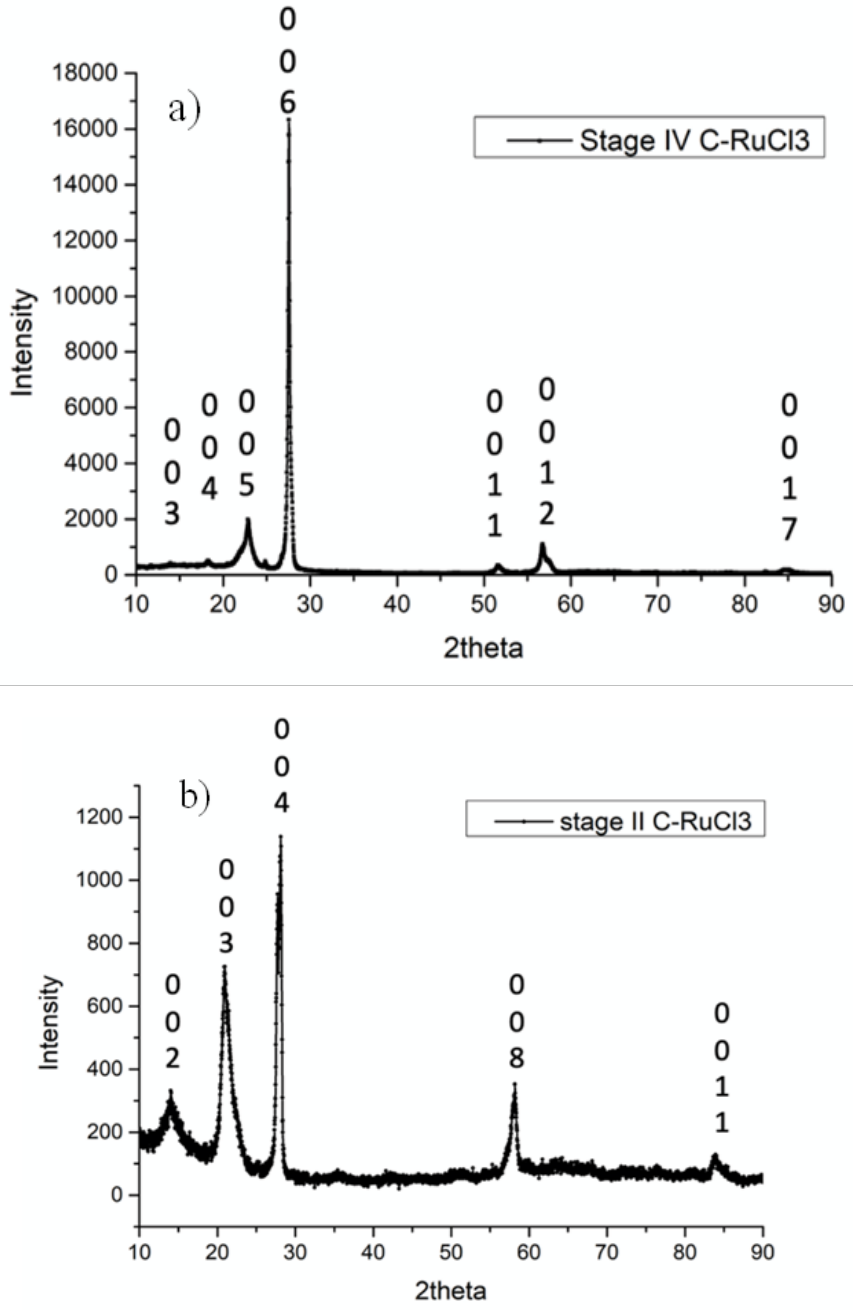

Figure 5.2-1 XRD pattern of stage-IV and stage-II intercalated Kish graphite. The Peak position is labeled by the Miller index.

The detailed calculation using the stage-II sample as an example process is as follows:

Starting with the d_{001} graphite (C-C distance), which is 3.353 Å, as shown in Figure 5.2-2 a), a box model of $RuCl_3$ intercalated graphite structure. In this model, we only consider the distance between layers while neglecting the thickness of the layer itself. The unit cell of the stage-II sample has two layers of graphite. Thus, there is only one box of C-C distance (blue box shown in Figure 5.2.2 a), in the united cell. The d_{00L} fitted from the position of the XRD peak is 12.7 Å. Then the distance between the graphite layer and $RuCl_3$ layer (green box) can be calculated as follows:

$$d_{C-RuCl_3} = \frac{(12.7 - 3.353)}{2} = 4{,}6735 \text{ Å}$$

While in the stage-IV sample, we have 4 layers of graphite in between, as we can see in Figure 5.2-2b). Thus, there are three C-C boxes in total. The thickness of graphite layers is 3 * 3.353 = 10.059 Å. Then we can calculate the d_{001} of the stage-IV sample by inserting the C-$RuCl_3$ distance calculated from the stage-II sample:

$$d^{cal}_{00l-stage\ IV} = 10.059 + 2 * 4.635 = 19.41 \text{ Å}$$

This number is closed to what we obtained from the experimental XRD result, which is a cross-proof of the rationality of this number.

With lattice parameter c and distance between graphite and $RuCl_3$ layer, we can simulate a possible structure of stage-II C-$RuCl_3$ as shown in 5.2-3. It is a simplified unit cell with least amount atoms in it.

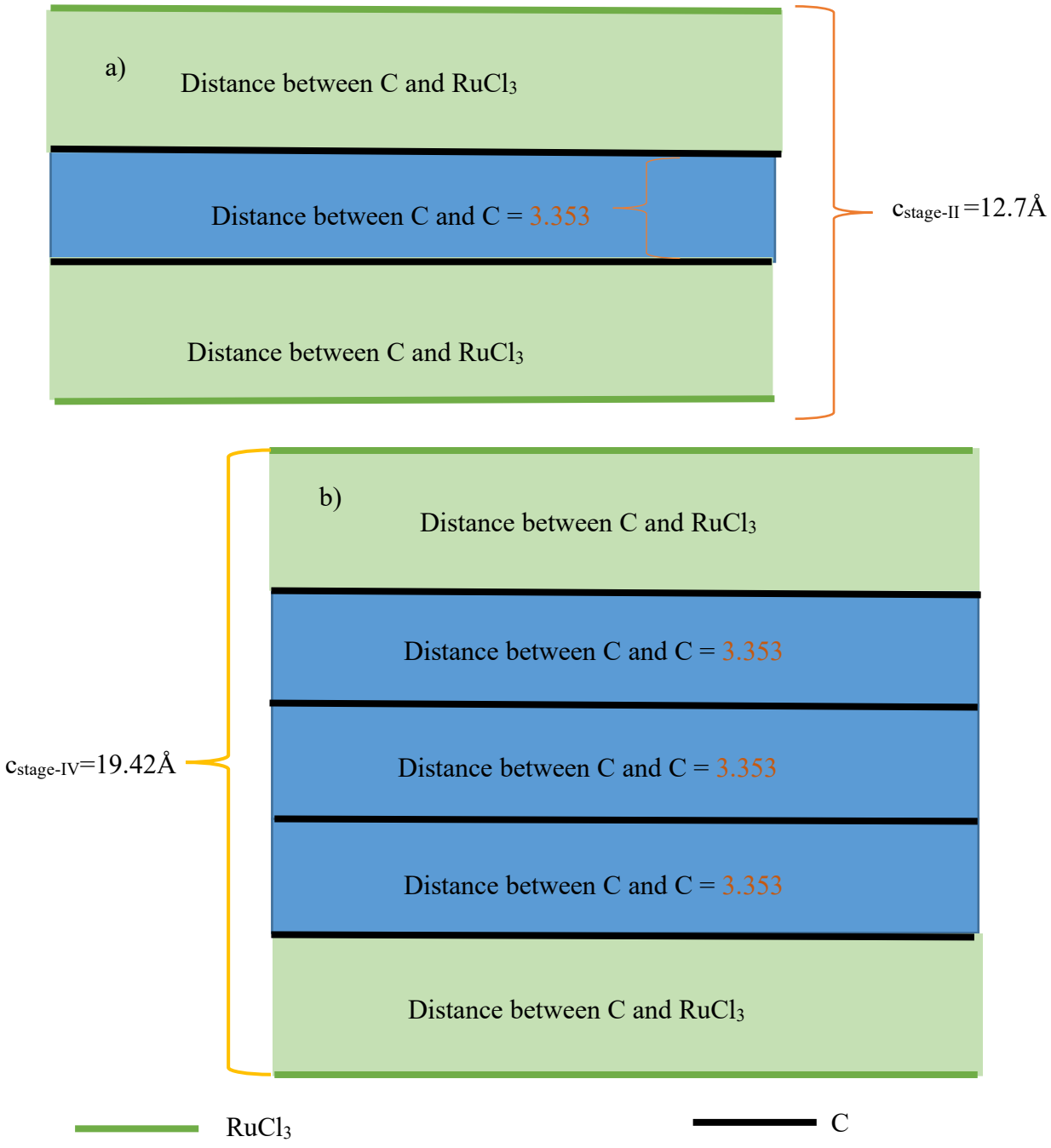

Figure 5.2-2 Box model representing the structure of a) stage II C-$RuCl_3$ sample. b) stage-IV C-$RuCl_3$. In the model, each box representing the distance between the different layers of crystal lattice. The blue box represented the C-C distance while green box is the distance between graphite and $RuCl_3$.

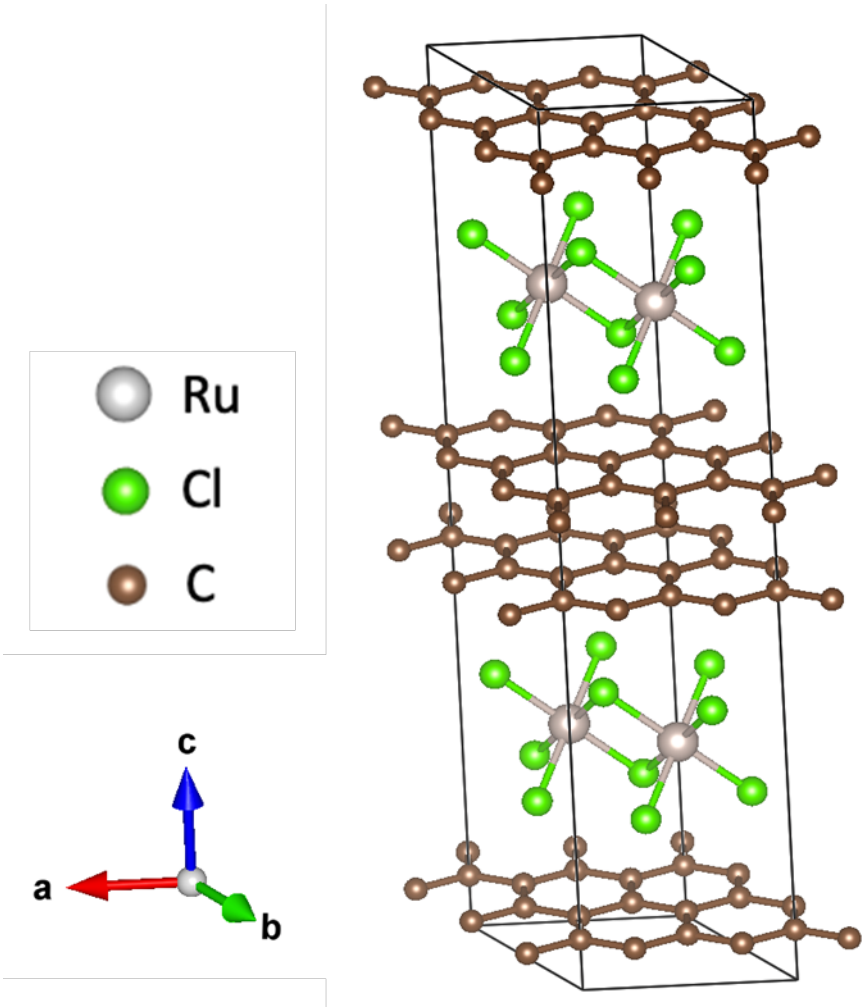

Figure 5.2-3 Proposed unit cell of stage-II C-$RuCl_3$ Here we have an assumption that the two graphite layers in between follows A-A stacking sequence.

5.3 High-pressure Synchrotron X-ray Diffraction and Structure Refinement

To better understand how the pressure will affect the crystal structure of C-$RuCl_3$, we performed the high-pressure synchrotron X-ray diffraction measurement on a piece of stage two sample.

The sample picked for high-pressure synchrotron X-ray diffraction was the first measure under the PXRD to confirm that it is the pure stage and characterized by PPMS to ensure the good quality of the sample. The picked sample was then cooled down to 77 K and crashed into small pieces. One small piece of proper size was transferred to a DAC and measured under a synchrotron XRD with a pressure applied range from 0.45 to 12.3 GPa.

5.3.1 Structure Assumptions and Criteria

Before we move on to the data analysis, we made several assumptions for the C-$RuCl_3$ sample's structure search.

All the assumptions are coming from the reference.

A. Considering the structure analogy to $FeCl_3$, $CrCl_3$, and $AlCl_3$-intercalated graphite in the reference we have the following assumptions [16], [17], [36], [38], [39], [42]–[44], [47], [53]. a). $RuCl_3$ crystallizes into a layered solid composed of $Cl_3Ru_2Cl_3$ intercalate sandwiches that are incommensurate with the graphite host. b). The basic molecular symmetry groups are preserved upon intercalation. Both graphene and $RuCl_3$ form trigonal symmetry. When C-$RuCl_3$ is in stage 2, the host has an orthorhombic Cmc21. c). Assume the graphene and $RuCl_3$ layers

form a supercell constructed by combining n × m unit cells of $RuCl_3$ and N × M of graphene. The XRD profiles of superlattices constructed by multiple local unit cells like C-$RuCl_3$ are the overlap of the {hkl} reflections from the local cells (main reflection) and superlattice (satellite reflection). Since the satellite reflections are much weaker (less intense) than main reflections, and the experimentally observed disorders, the satellite peaks are expected to be invisible. Thus, we first handle the host and guest structures separately, investigating only the main reflections. Then, we build the superlattice and do the final check.

d). The coupling between the graphene layers and $RuCl_3$ layers is weak. The crystal lattice constants in the host and guest layers do not change significantly upon intercalation.

i. C-C distance ($d_{C\text{-}C}$) in graphene: 1.42 Å

ii. Inter-layer distance between adjacent graphene (C0): 3.35 Å

iii. Ru-Cl ($d_{Ru\text{-}Cl}$) distance in $Cl_3Ru_2Cl_3$: 4.6735 Å

iv. Distance between two graphene layers that sandwich $RuCl_3$ (ds): > 9 Å

e). The contribution from the $RuCl_3$ lattice is dominant in the observed XRD peak intensity (The XRD scattering intensity is proportional to the square of atomic numbers. C12, Ru44, Cl17). For the fully intercalated sample, XRD observes the structure of $RuCl_3$.

f). Two adjacent graphene layers stack as AB, AC, or BC (Natural graphite has ABAB or ABCABC stacking). Two graphene layers that sandwich $RuCl_3$ in between stack AA, BB, or CC.

B. XRD (Figure. 5.3-1) observed diffuse scatterings near the XRD peaks, indicating the presence of significant disorders, including domains, in a crystal or a phase mixing with different stages. a) Assume that the disorders (or atomic positions vacancies) in layers smeared and broadened the XRD peaks. b) The intercalants do not wholly occupy the inter-layer space due to the intercalation nature. So, I assume the disorders are mostly in $RuCl_3$ layers. Thus, the hkl ($h \neq 0, k \neq 0$) reflections indicate more diffuse scattering while 00l reflections do not so much.

C. XRD image (Fig. 5.3-1) shows a preferred orientation., Thus, The XRD peak intensity ratio in the XRD profiles is not very accurate.

There are two types of the orientation of a graphene layer relative to a $RuCl_3$ layer, depending on how to set the unit cells (Figure5.3-2). It gives us two C-$RuCl_3$ ratios The structure models where the analysis starts are listed in Table 5.3-1.

5.3.2 XRD Data Analysis

Figure 5.3-3 shows the simulated XRD profiles for all eight models listed in table 5.3-1 at 1 bar and the experimental data at 0.43 GPa. The XRD profiles between the same stages are identical because the XRD observes mostly the diffraction from the guest's lattice. The apparent difference between the stages is in the peak positions at $2\Theta \sim 3.5$ deg. Each model of stage 2 and above has an intense peak, while models of stage1 and experimental XRD data do not. Those intense peaks should be observable even with a significant lattice disorder. Therefore, I exclude stages 2-4 from candidates.

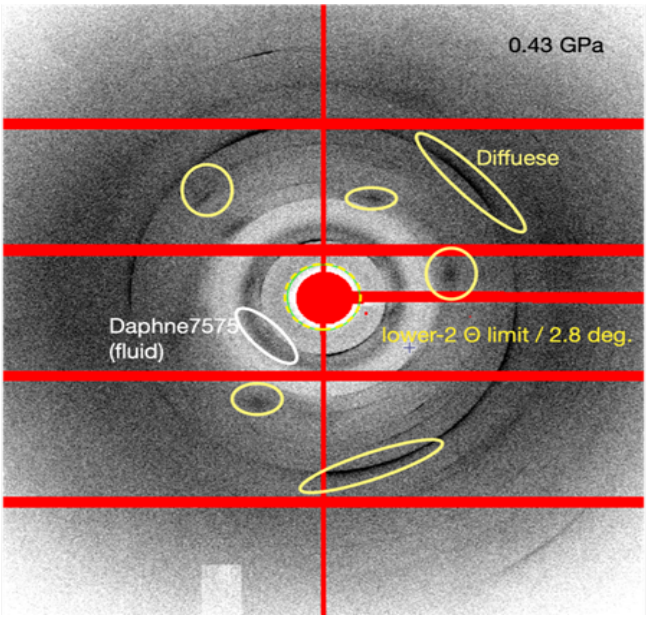

Figure 5.3-1 XRD image recorded on a detector array. A red circle and a rectangle are the shadows of a direct X-ray beam stopper and a holder. Due to the direct beam stopper, the lower limit of the 2Θ is 2.8 deg. Red rectangle is the blank between detectors. Yellow ovals indicate the broad and diffused XRD signals. The scattering from Daphne7575 oil is indicated with white oval.

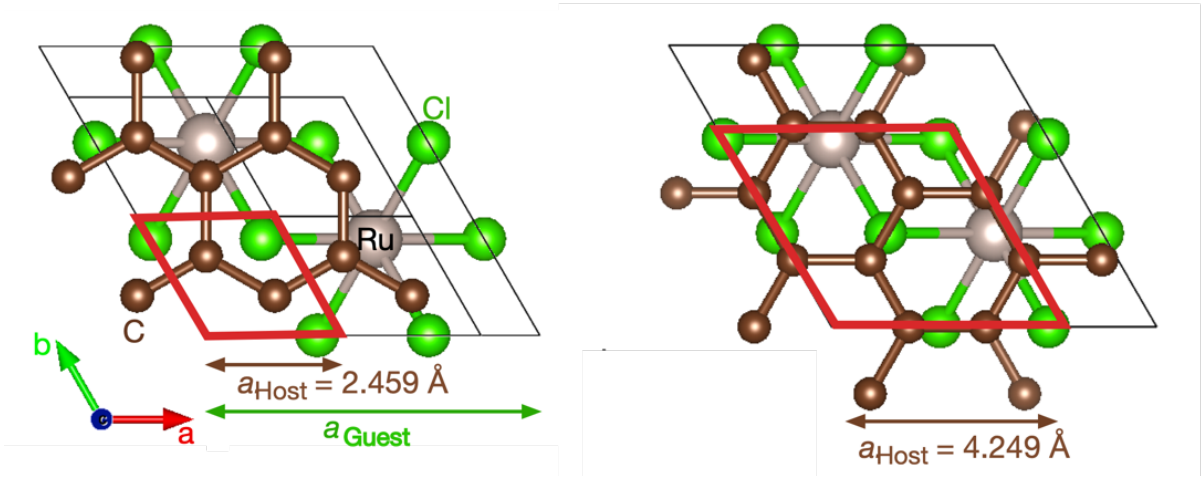

Figure 5.3-2 Two orientations of graphene layers.

Table 5.3-1 Structure Models of Host and Guest to Start the Analysis.

	stage	stacking	Symmertry and lattice constants
1	I	¦|A¦A¦|	*P-31m* (a = 2.456 Å, c = 10.248 Å, α = β = 90˚, γ = 120˚)
2		¦|A¦A¦|	$P6_3/mmc$ (*a* = 4.249 Å, *c* = 10.248 Å, *α* = *β* = 90˚, *γ* = 120˚)
3		¦|A¦A¦|	$P6_3/mmc$ (*a* = 2.456 Å, *c* = 20.470 Å, *α* = *β* = 90˚, *γ* = 120˚)
4		¦|A¦A¦|	*R-3m* (*a* = 4.249 Å, *c* = 30.600 Å, *α* = *β* = 90˚, *γ* = 120˚)
5	II	|A¦AB¦B|	$P6_3/mmc$ (*a* = 2.456 Å, *c* = 30.797 Å, *α* = *β* = 90˚, *γ* = 120˚)
6		|A¦AC¦CB¦B	*R-3m* (*a* = 2.456 Å, *c* = 46.090 Å, *α* = *β* = 90˚, *γ* = 120˚)
7	III	|A¦ABAC¦CA|	$Cmc2_1$ (*a* = 2.456 Å, *b* = 4.260 Å, *c* = 41.000 Å, *α* = *β* = 90˚, *γ* = 120˚)
8	IV	|AB¦BCAB¦BC|	*R-3m (a = 2.456 Å, c = 60.600 Å, α = β = 90˚, γ = 120˚)*

¦: intercalants

|XXXXX|: unit cell

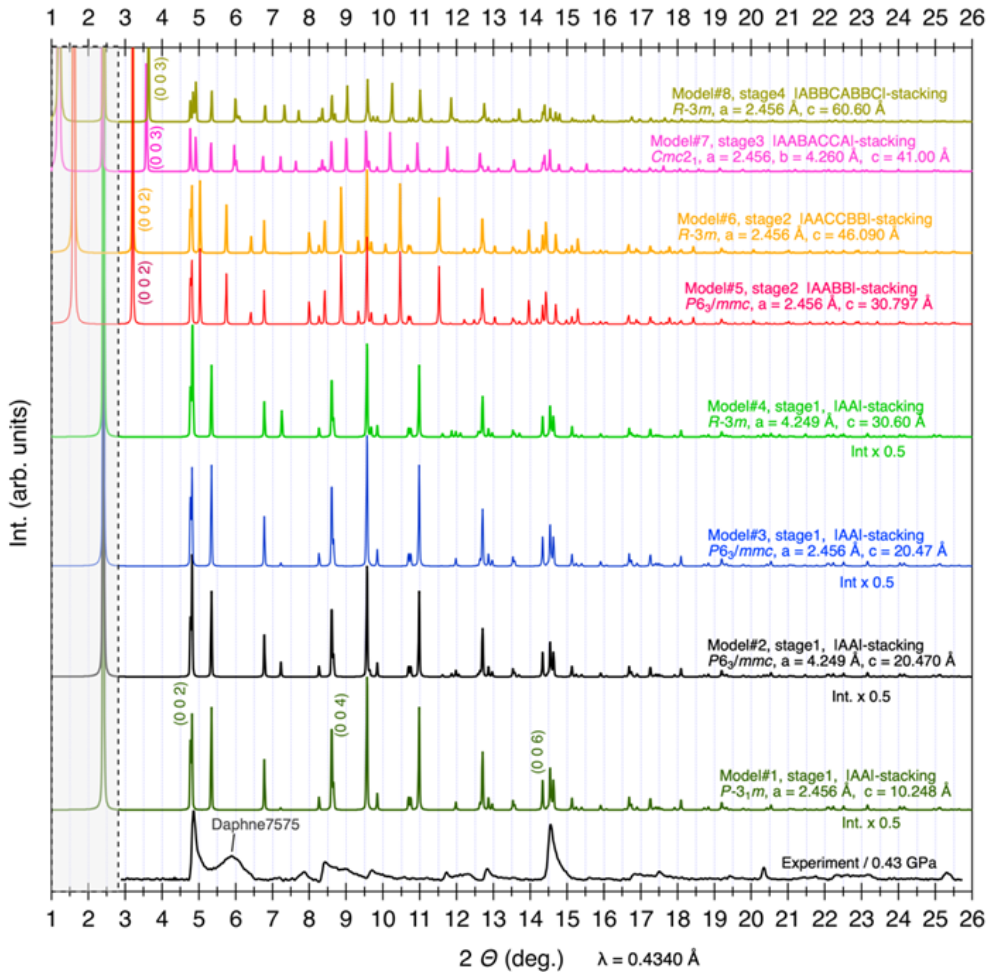

Figure 5.3-3 Simulated XRD profiles for Model #1-8 at 1 bar and the experimental data at 0.43 GPa. The experimental data is after background subtraction. NOTE: The XRD simulation assumes a stoichiometric sample without any disorders.

Figure 5.3-4 is the comparison of XRD profiles between stage1 models. Model #3 and Model #4 are geometrically the same as Model #1 and Model #2, respectively. Here, Fig. 5.3-5 compares the profiles of Model #1 and Model #3. In the XRD profile, the difference between Model #1 and Model #3 is barely visible. We performed the lattice constants (a, b, and c) refinement Models odel#1 and #3.

The lattice constant refinement does the peak fitting to the experimental data. Here, we intentionally ignore the peak intensity ratio and consider only peak positions because of the peak broadening and preferred orientation in the XRD data. The peak fitting function's FWHH is set 1- 1.5 deg., considering peak broadening.

It is noted that XRD detected the possible presence of non-intercalated graphite or some other layered structure. At the current moment, we temporarily define it as non-intercalated graphite. In this graphite, its c-axis is 0.36 Å shorter than ambient pressure and corresponds to 2.5 GPa, while its a-axis does not change. It may reflect that there are pure-graphite domains under a uniaxial compression by the surroundings. Otherwise, there might be some other phase of C-$RuCl_3$.

The host structures' symmetries, *P-31m* of Model #1 and *P63/mmc* of Model #3 can be reduced to *P3*, which is the same as the guest. The superlattices for the two structures are built by merging the host and guest into single-unit cells. Table 5.3-2 is the list of lattice constants of possible host and guest structure combination.

The result structure models will be discussed in the following section.

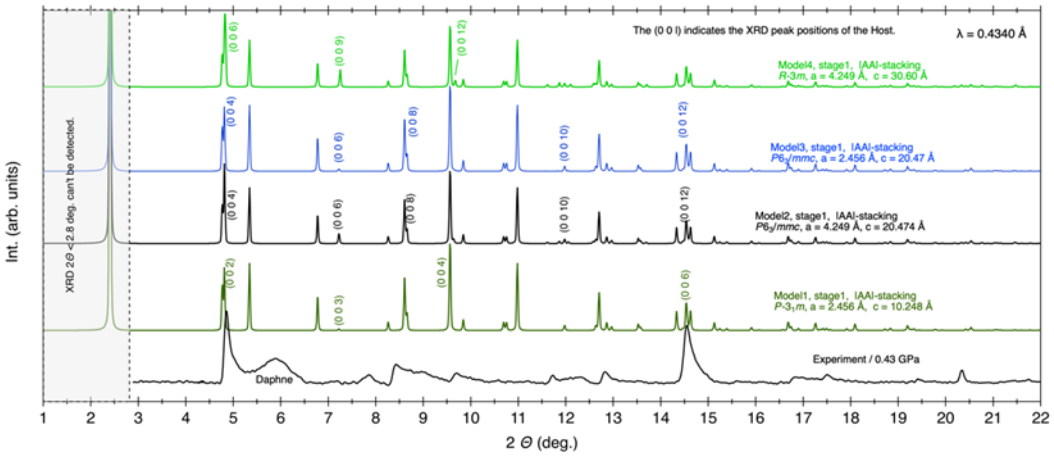

Figure 5.3-4 Comparison of XRD profiles between stage1 models. The (00l) are the peak positions from the host lattice. NOTE: The XRD simulation assumes stoichiometric samples without any disorders.

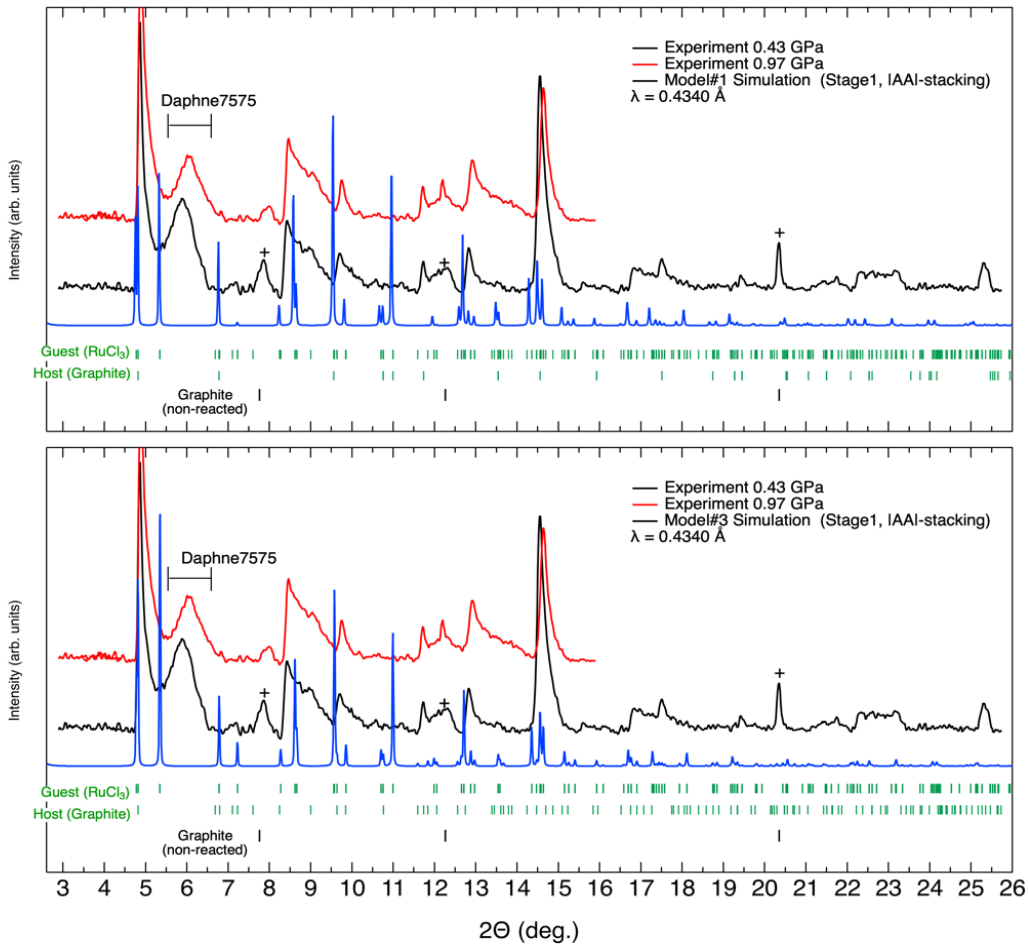

Figure 5.3-5 The peak position comparison between the experimental data with Model #1and Model #3 after crystal lattice constants fitting (least-square fitting). Green lines indicate the XRD peak positions.

NOTE: The XRD simulation assumes a stoichiometric sample without disorders and preferred orientation.

Table 5.3-2 Lattice Constants for Host and Guest in C-$RuCl_3$ (stage-I) at 0.43 GPa.

Model #	**phase**	**symmetry**	**lattice constants**
1	Host	*P*-31*m*	$a = b = 2.456 \pm 0.003$ Å, $c = 10.23 \pm 0.02$ Å, $\alpha = \beta = 120^\circ$, $\gamma = 120^\circ$
	Guest	*P*3	$a = b = 5.973 \pm 0.04$ Å, $c = 10.25 \pm 0.09$ Å, $\alpha = \beta = 90^\circ$, $\gamma = 120^\circ$
2	Host	$P6_3mmc$	$a = b = 4.255 \pm 0.003$ Å, $c = 20.51 \pm 0.01$ Å, $\alpha = \beta = 120^\circ$, $\gamma = 120^\circ$
	Guest	*P*3	$a = b = 5.970 \pm 0.004$ Å, $c = 10.23 \pm 0.01$ Å, $\alpha = \beta = 90^\circ$, $\gamma = 120^\circ$

5.3.3 Structure Models

The structure models with superlattice can be constructed by combining the unit cells of graphene and RuCl3. Model #1 possess the superlattice that is 12 × 12 × 1 unit cell of graphene and 5 × 5 × 1 of RuCl3. Model #3 is 7 × 7 × 1 unit cell of graphene and 5 × 5 × 1 of RuCl3. Note that the lattice constants in the model were adjusted to exactly match the superlattice's lattice constants. Those ratios are coming from different rotation pattern of graphite.

Figure 5.3-7 shows the reconstructed structure models and the simulated XRD profile. The main (strong) XRD peak positions do not change Model #1 and Model #3. However, the peak intensity ratio changes and the satellite peaks appear for Mode #3 (2Θ at around 6 − 9˚).

Table 5.3-3 lists the lattice parameter of most possible structures represented as Model #1S and Model #3S.

5.4 Scanning Electron Microscope Measurement

SEM measurement has been carried out to confirm the existence of $RuCl_3$ using a high voltage (30 kV) setup. A pure $RuCl_3$ single crystal has been put into the chamber and measured under the same condition.

Both of them showed a little peek at ~19.3 kV, which is the kb energy of Ru. This is strong evidence of the existence of Ru element as well as Cl element in the sample.

The reason we were using a 30 kV setup is that The Highest peak on the EDS pattern belongs to both the Cl element and Ru element. Ru and Cl elements coincidentally have a similar characteristic spectral line.

Table 5.4-1 Lattice Constants of Possible Structure of C-$RuCl_3$ (stage-I) at 0.43 GPa.

Model#	**symmetry**	**lattice constants**
Model#1S	*P*3	$a = b = 29.8125$ Å, $c = 10.241$ Å, $\alpha = \beta = 120^\circ$, $\gamma = 120^\circ$
Model#3S	*P*3	$a = b = 29.8125$ Å, $c = 10.241$ Å, $\alpha = \beta = 120^\circ$, $\gamma = 120^\circ$

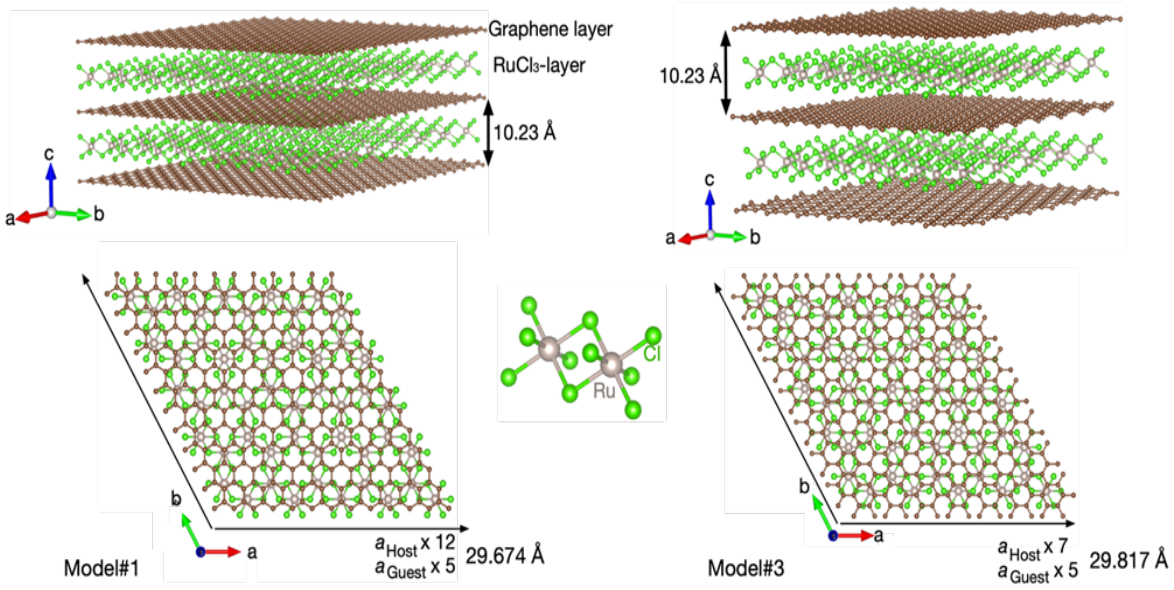

Figure 5.4-1 The superlattice structure of Model #1 and Model #3 after lattice parameters refinement. The supercell is constructed by combining 5 × 5 unit cells of $RuCl_3$ and 12 × 12 of graphene for Model #1. Model #3 is 7 × 7 unit cells of $RuCl_3$ and 5 × 5 of graphene.

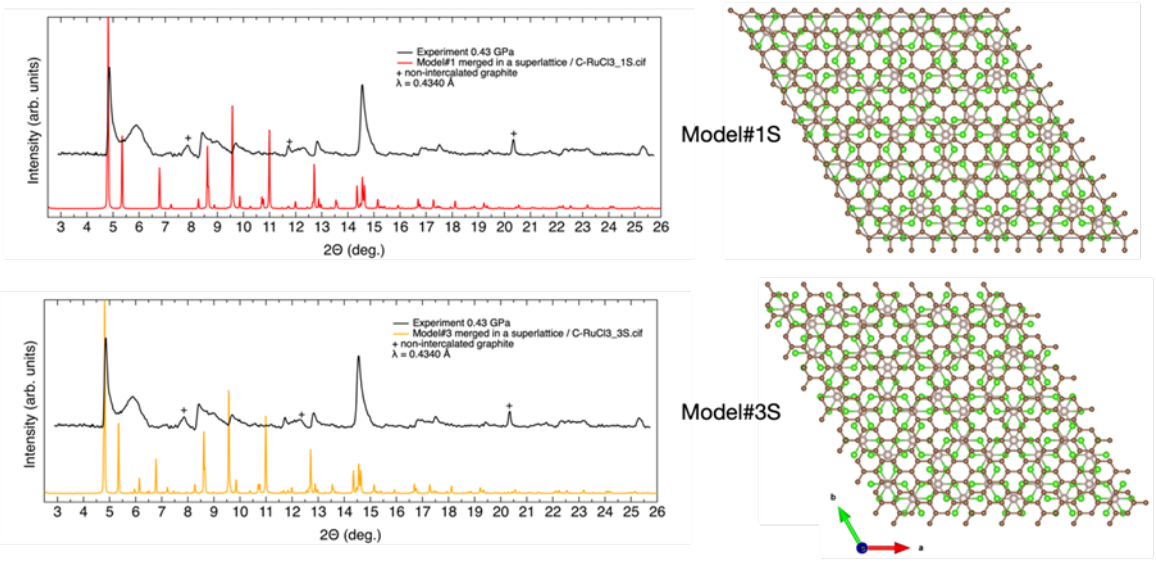

Figure 5.4-2 (Top R and L) Reconstructed structure model for Model #1S and 3S and the simulated XRD profiles for the reconstructed structure models. NOTE: The XRD simulation assumes a stoichiometric sample without disorder and preferred orientation. Thus, the XRD peak intensity ratio should be different from the experimental data. Also, note the difference in the orientation of the graphene layer between Model #1S and #3S.

Thus, their highest spectrum peak (Ru-La/Cl-Ka) overlapped with each other, as shown in Figure 5.4-1. Thus, we cannot distinguish them by just looking at the peak around 2.6 keV. After applying higher voltage, we caught the Ka energy of Ru shown as a small peak at ~19.3 keV (see Figure.5.4-1). Since the background noise cannot be seen on both the left side and right side of this peak, we can also conclude that this peak is not coming from the background noise.

SEM image was captured on the surface of the $RuCl_3$ intercalated graphite with EHT set at 12 kV. We can see a clear laminar structure and hexagonal shape hole. The hole comes from the surface energy concentrated during the annealing process. This hexagonal shape also indicated a honeycomb lattice unit cell of this kind of material

5.5 Raman Scattering Measurements of C-$RuCl_3$

We performed Raman scattering measurement of C-$RuCl_3$ at ambient pressure and room temperature. The sample was stage-I and III mixed. We measured three positions in the sample and observed consistent Raman scattering spectra at all positions. In the Figure 5.5-1, 'G' indicates the vibrational modes that are characteristically observed in graphite. The peak at 1600 cm-1 consists of D (E2g-symmetry) and G (A1g-symmetry) modes. 2700 cm^{-1} is 2D (2nd harmonic). This result indicates that the sample has some disorder in its structure, and the intercalation of $RuCl_3$ possibly induces the disorder.

This disorder was also observed and cross proved as broadened peak at low angle in the X-ray measurement.

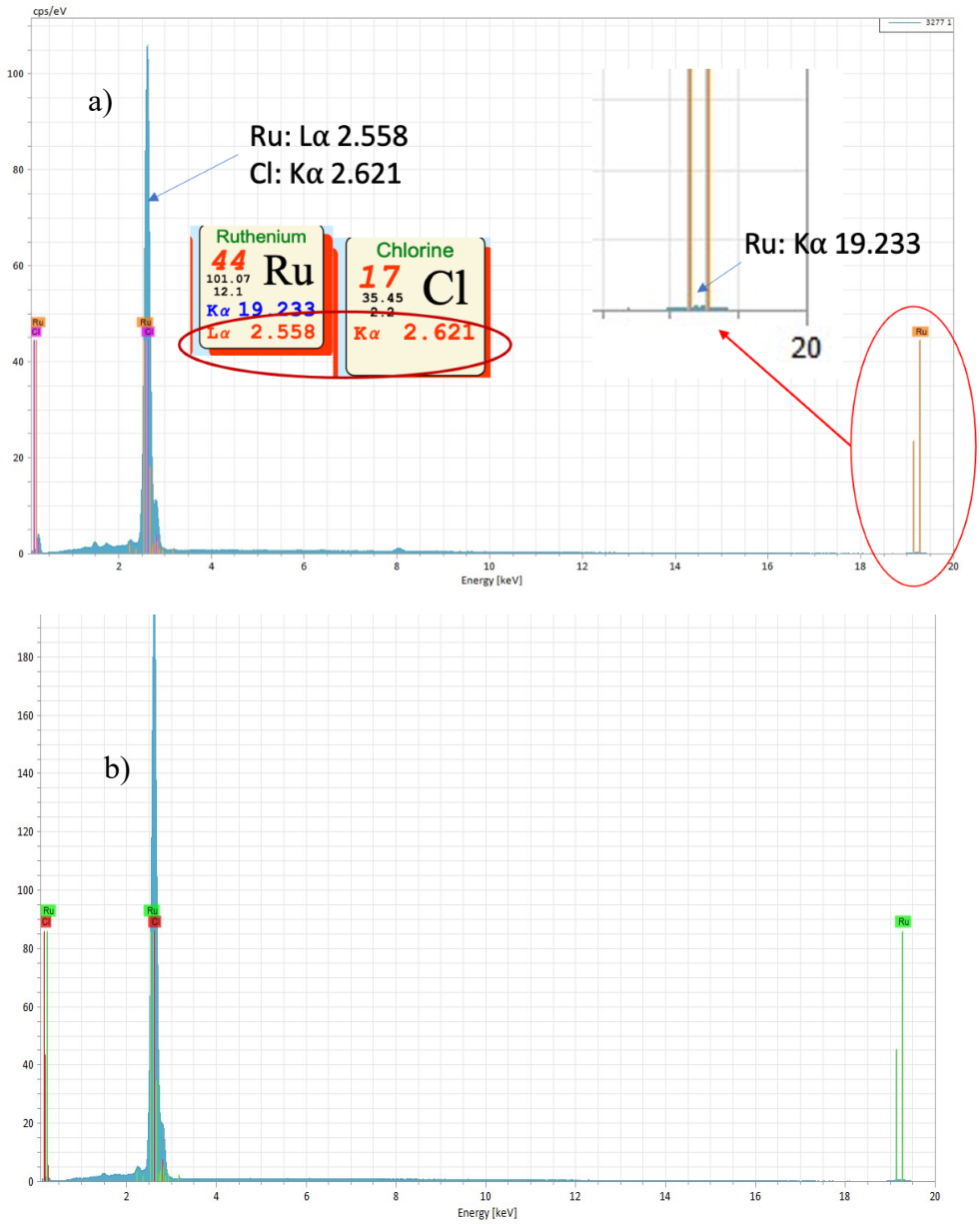

Figure 5.5-1 a) EDX spectrum measured at 30 kV. The background signal cannot be seen at high energy while we do see some signals at 19.3 keV. b) Spectrum of pure single crystal $RuCl_3$ measured at 30 kV. It has the same behavior as C-$RuCl_3$ sample at 16-20 keV section. Which is a cross proof of existence of $RuCl_3$ in the C-$RuCl_3$ sample.

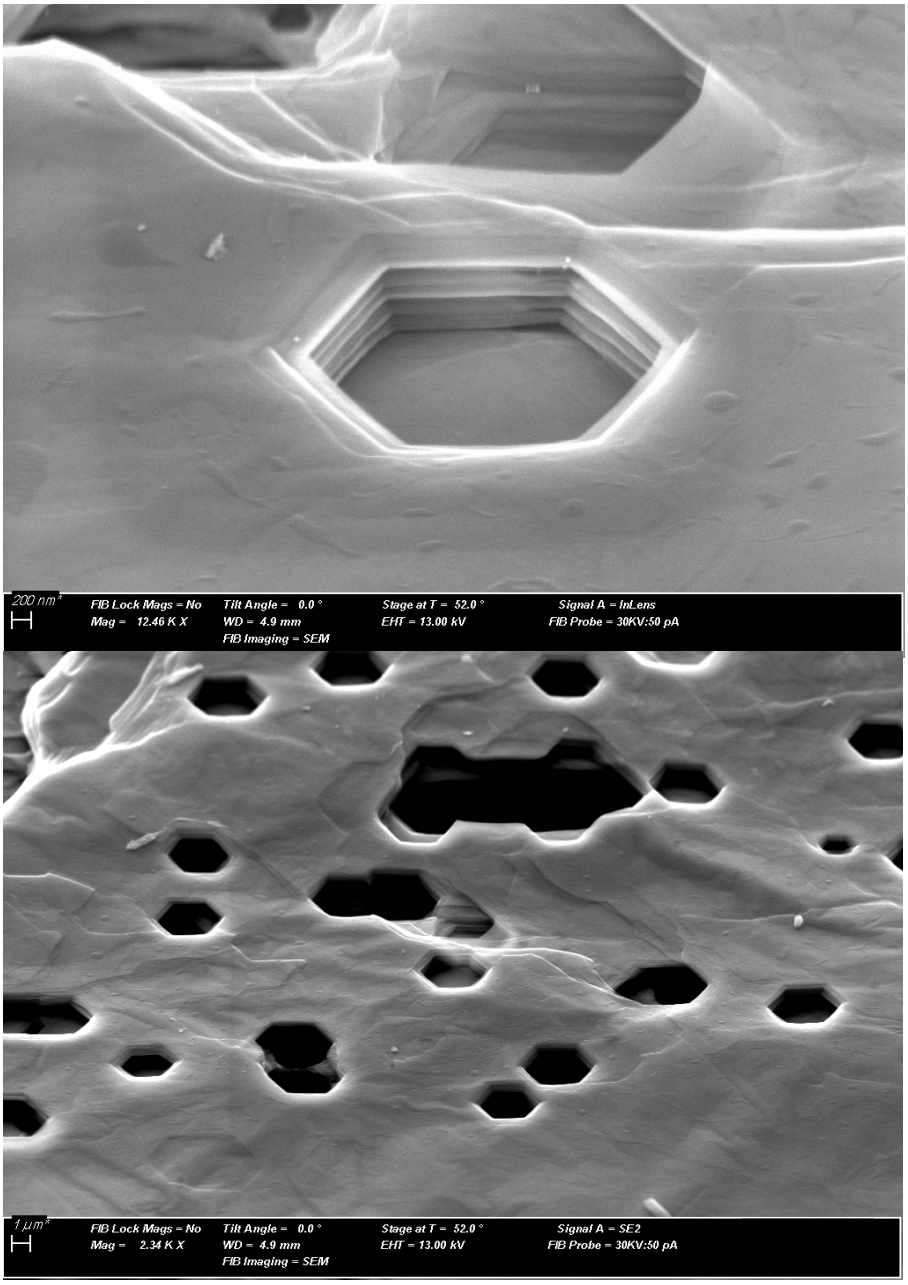

Figure 5.5-2 Scanning Electron Microscope image on the surface of C-$RuCl_3$.

We can see clear layered and hexagonal structure.

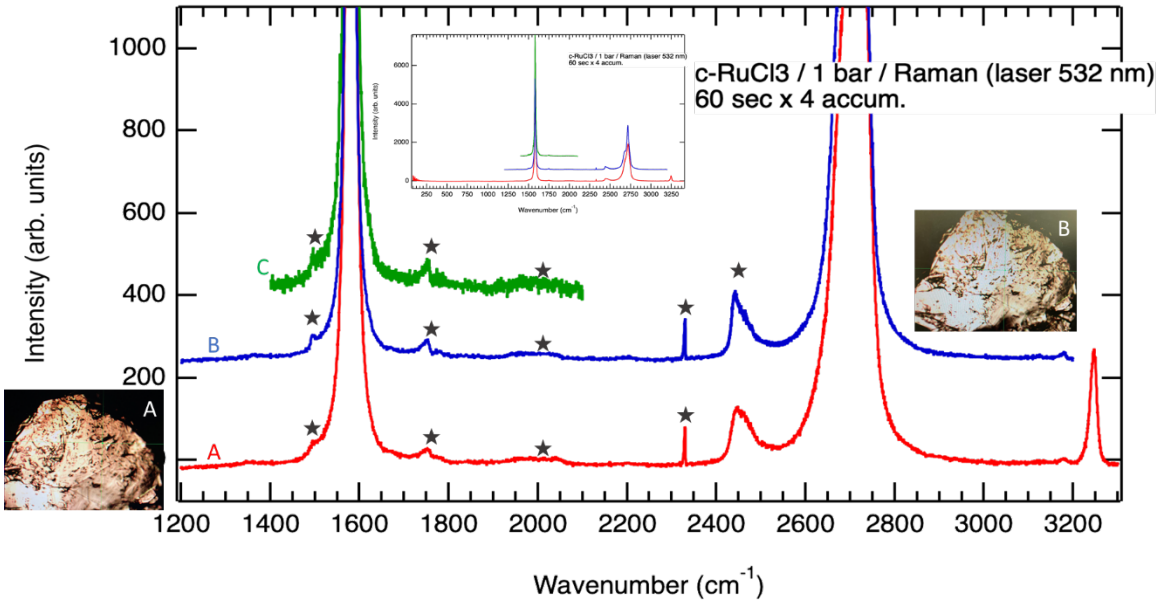

Figure 5.5-3 Raman scattering spectra of c-$RuCl_3$ (sample C, stage I-II mixed) at 1 bar and 300 K. We performed measurements on 3 different positions (A-C). The ★ indicates the modes that are not observed for pure graphite.

5.6 Transport Properties Measured by PPMS

Transport properties have been measured using Physical Property Measurement System. We measured resistivity as a function of Temp and field on several pieces of stage-II and stage-IV samples, as well as pure graphite as a reference. The referenced graphite was also annealed under a chlorine atmosphere at 900 ˚C in the sealed tube without a $RuCl_3$ pellet for several days to eliminate the potential effect of other conditions. The magnetoresistance of the stage-IV sample showed oscillations above 4 T as shown in Figures 5.6-1,5.6-2. By performing a fast Fourier transformation, we identify the frequency of oscillations for the $RuCl_3$ intercalated graphite at frequencies of ~ 91 T and 176 T, which is different from what we observed in pure graphite, as shown in Figure 5.6-3. The oscillations that we are seeing are coming from the modified Fermi surface of graphite (due to $RuCl_3$ intercalation). The intercalation process improves the crystalline quality because the intercalated sample had a more pronounced oscillation behavior. A Hall resistivity of the stage-II sample has been measured as well. The sample was hole-doped with a density of around $7.8 * 10^{20}$ cm^{-3}.

5.7 Resistivity under Pressure

We found that the intercalate graphite is sensitive to pressure. Even a small pressure will change the structure of the intercalating stage. Thus, we designed an experiment in which we applied different pressure while measuring the resistance of a piece of mixed stage sample.

As shown in the Figure. 5-7.1, The resistance first increases, then dope. At a pressure over 4.6 GPa, the sample's resistance rocketed up and seemed to be more semiconducting. The sp^3 bonding may be formed, making a hexagonal diamond

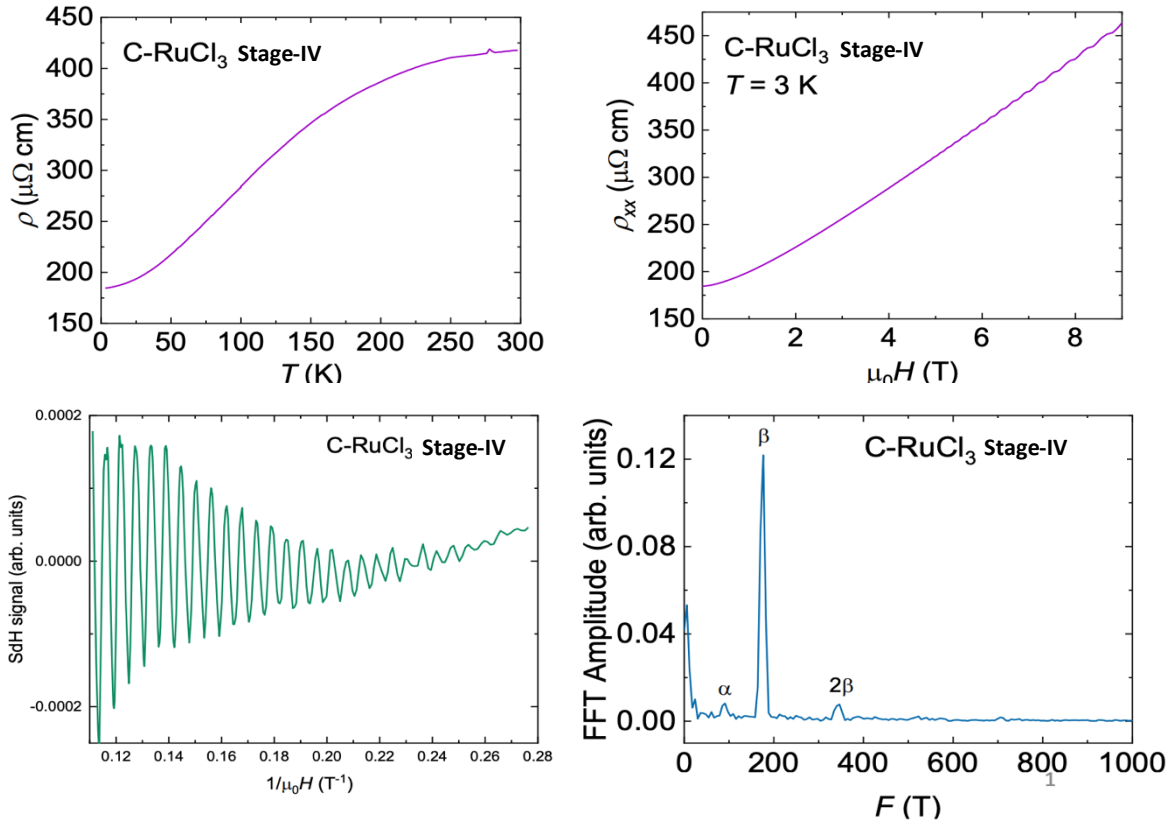

Figure 5.7-1 Magnetoresistance measurement on stage IV C-$RuCl_3$ sample. (Top-left) Magnetoresistance as a function of temperature. (Top--right) Magnetoresistance vs. applied magnetic field. (Bottom-left) Shubnikov–de Haas oscillation. (Bottom-right) Fast Fourier transformation analysis of the oscillatory magnetoresistance.

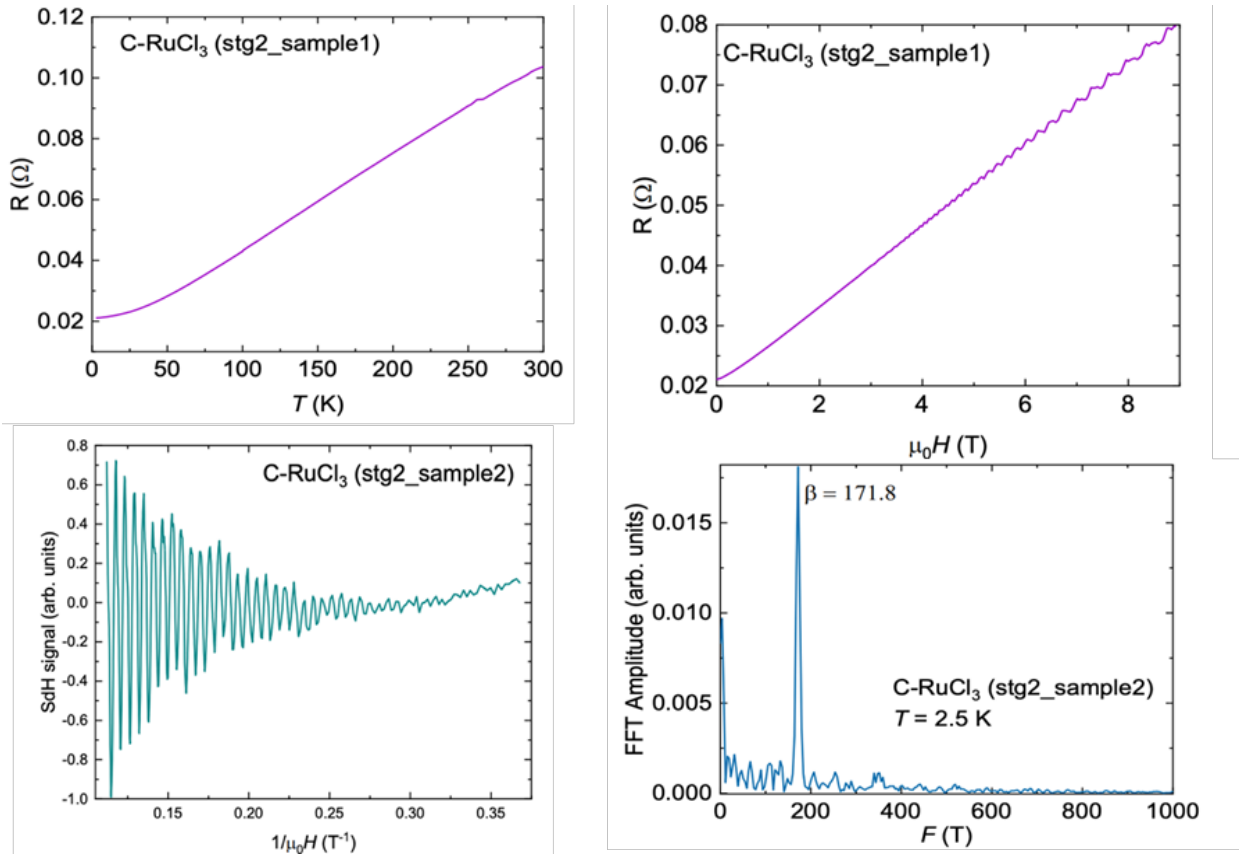

Figure 5.7-1 Magnetoresistance of stage-II sample. (Top-left) Magnetoresistance as a function of temperature. (Top--right) Magnetoresistance vs. applied magnetic field. (Bottom-left) Shubnikov–de Haas oscillation. (Bottom-right) Fast Fourier transformation analysis of the oscillatory magnetoresistance.

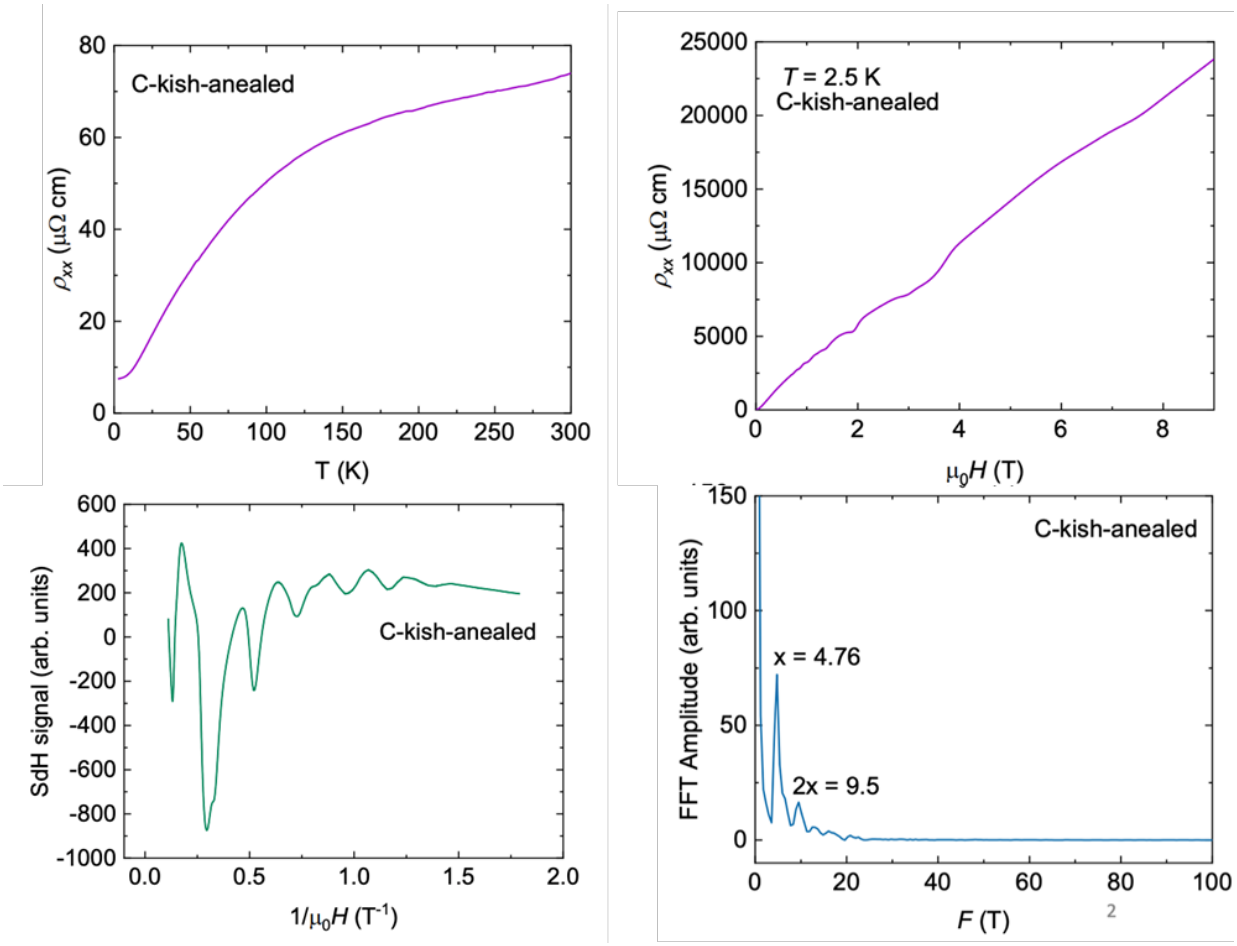

Figure 5.7-2 Magnetoresistances of annealed kish graphite. (Top-left) Magnetoresistance as a function of temperature. (Top--right) Magnetoresistance vs. applied magnetic field. (Bottom-left) Shubnikov–de Haas oscillation. (Bottom-right) Fast Fourier transformation analysis of the oscillatory magnetoresistance.

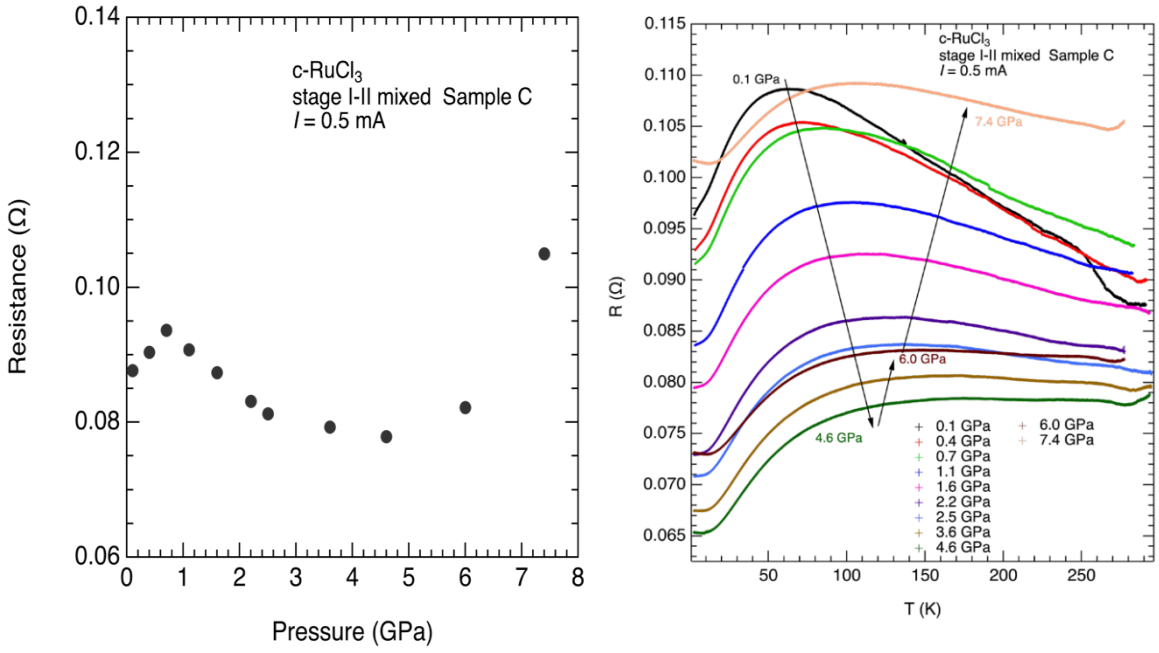

Figure 5.7-3 (Left) Resistance vs. pressure measured on mixed stage I-II C-$RuCl_3$. (Right) Resistance vs. temperature on mixed stage I-II C-$RuCl_3$ indicated pressures.

CHAPTER 6. CONCLUSIONS AND FUTURE WORK

6.1 Conclusions

To design a possible candidate of Kitaev material, there are two requirements that need to be achieved. One is bond directional dependent Ising-coupling, which can lead to an exchange frustration. The second one is a ground state of spin = 1/2. That requires a honeycomb lattice or a Kagome shape lattice and a half-filled d electron. In this work, Inspired by the first generation Kitaev spin liquid material: A_2MO_3 and $RuCl_3$, two different second-generation Kitaev materials: new delafossite honeycomb material $A_3BM_2O_6$ where A =Ag, Cu; B = Li, Na; M = Ru, Rh, Ir. and $RuCl_3$ intercalated graphite. The delafossite material was synthesized using a low-temperature ion-exchange method. We successfully grow $Ag_3LiRu_2O_6$, $Ag_3LiRh_2O_6$, $Ag_3LiIr_2O_6$, $Cu_3NaIr_2O_6$, and $Cu_3LiIr_2O_6$ samples. A detailed investigation was carried out on $Ag_3LiRh_2O_6$, $Ag_3LiIr_2O_6$, sample, XRD pattern showed a clear Warren shape indicate a stacking fault in this material. Fractional miller indices of (1/3, 1/3, l) where l is an arbitrary integer was obtained by the position of a barren-shape peak on the pattern high-temperature XRD showed the time and annealing temperature correlational relationship in the ion-exchange process. The STEM image showed a quasi-layered, alternating arrangement of $[LiRuO_4]^-$ octahedra and Ag atoms. The magnetic measurement confirmed the Antiferromagnetic behavior of both two samples. We observed a magnetic peak with a Miller index of (1/6, 1/6, l) which is half of the index of Warren shape peak. This phenomenon indicated that the magnetic order of this material originates from the part of the sample that produces the Warren-line shape. Also, based on the fact that the magnetic unit cell doubled along the a and b axis, we proposed that this material has a zig-zag magnetic model.

For halide intercalated graphite material, we successfully grow different stages of C-$FeCl_3$, C-$MnCl_2$, C-$CuCl_2$, and C-$RuCl_3$. Different from another intercalated graphite sample, C-$RuCl_3$ has a strict requirement of the chlorine atmosphere pressure to trigger the intercalation. Then we invented a new three-zone method to introduce chlorine atmosphere into the sealed system by utilizing photosensitive material AgCl and UV light. Pure stage-II and stage-IV C-$RuCl_3$ samples were obtained using this method, proved by XRD measurement. Lattice parameter c was derived from the 00l peak position. With proper assumption, we also calculated the distance between the graphite layer and $RuCl_3$ layer and proposed a stage-II sample unit cell. The high-pressure synchrotron XRD showed that the sample's structure is sensitive to pressure. The structure turned to stage-I after applying a small pressure. By analyzing and refining the XRD data, we also proposed a proper superlattice of the stage-I sample. This sensitivity has been cross proved by the high-pressure resistivity measurement. The resistivity rockets up and then gradually drop with the applying pressure increase. The transport measurement on both stage-II and stage-IV samples showed beautiful quantum oscillation above 4T. This oscillation may come from the modified Fermi surface of graphite due to the intercalation of $RuCl_3$

Theoretical DFT calculation was carried out based on the proposed unit cell. The density of state was calculated using the PBE exchange-correlation functional. More work is on the way.

6.2 Recommendations for Future Work

In the future, we can do more transport measurements on the analogy of C-$RuCl_3$, for example, the C-$FeCl_3$, C-$CuCl_2$, C-RuI_3.etc to see if the quantum oscillation overserved in the C-$RuCl_3$ sample is a feature of this group of material or C-$RuCl_3$ itself.

Try to make a stage-I $RuCl_3$ sample. It should have a more interesting behavior due to its metal-insulator alternating structure.

Carry out a detailed investigation on Cu-based delafossite material.

LIST OF REFERENCES

[1] Kitaev, A.Y., 2003. Fault-tolerant quantum computation by anyons. Annals of Physics, 303(1), pp.2-30.

[2] Jackeli, G. and Khaliullin, G., 2009. Mott insulators in the strong spin-orbit coupling limit: from Heisenberg to a quantum compass and Kitaev models. Physical Review Letters, 102(1), p.017205.

[3] Wan, X., Wang, Z. and Yang, K., 2013. From the fractional quantum Hall effect to topological quantum computation. Wuli, 42(8), pp.558-566.

[4] Moore, G.E., 1998. Cramming more components onto integrated circuits. Proceedings of the IEEE, 86(1), pp.82-85.

[5] Landauer, R., 1961. Irreversibility and heat generation in the computing process. IBM Journal of Research and Development, 5(3), pp.183-191.

[6] Shor, P.W., 1999. Polynomial-time algorithms for prime factorization and discrete logarithms on a quantum computer. SIAM Review, 41(2), pp.303-332.

[7] Willett, R.L., Nayak, C., Shtengel, K., Pfeiffer, L.N. and West, K.W., 2013. Magnetic-field-tuned Aharonov-Bohm oscillations and evidence for non-Abelian anyons at $\nu = 5/2$. Physical Review Letters, 111(18), p.186401.

[8] Chiaverini, J., Leibfried, D., Schaetz, T., Barrett, M.D., Blakestad, R.B., Britton, J., Itano, W.M., Jost, J.D., Knill, E., Langer, C. and Ozeri, R., 2004. Realization of quantum error correction. Nature, 432(7017), pp.602-605.

[9] Hermanns, M., Kimchi, I. and Knolle, J., 2018. Physics of the Kitaev model: fractionalization, dynamic correlations, and material connections. Annual Review of Condensed Matter Physics, 9, pp.17-33.

[10] Wen, X.G., 1995. Topological orders and edge excitations in fractional quantum Hall states. Advances in Physics, 44(5), pp.405-473.

[11] Savary, L. and Balents, L., 2016. Quantum spin liquids: a review. Reports on Progress in Physics, 80(1), p.016502.

[12] Shimizu, Y., Miyagawa, K., Kanoda, K., Maesato, M. and Saito, G., 2003. Spin liquid state in an organic Mott insulator with a triangular lattice. Physical Review Letters, 91(10), p.107001.

[13] Banerjee, A., Bridges, C.A., Yan, J.Q., Aczel, A.A., Li, L., Stone, M.B., Granroth, G.E., Lumsden, M.D., Yiu, Y., Knolle, J. and Bhattacharjee, S., 2016. Proximate Kitaev quantum spin liquid behaviour in a honeycomb magnet. Nature Materials, 15(7), pp.733-740.

[14] Millman, S.E. and Zimmerman, G.O., 1983. Observation of spin glass state in $FeCl_3$: intercalated graphite. Journal of Physics C: Solid State Physics, 16(4), p.L89.

[15] Nicholls, J.T., Murayama, C., Takahashi, H., Mōri, N., Tamegai, T., Iye, Y. and Dresselhaus, G., 1990. Magnetic properties of $CoCl_2$-graphite intercalation compounds under pressure. Physical Review B, 41(8), p.4953.

[16] Charlier, A., Charlier, M.F. and Fristot, D., 1989. Binary graphite intercalation compounds. Journal of Physics and Chemistry of Solids, 50(10), pp.987-996.

[17] Dresselhaus, M.S. and Dresselhaus, G., 2002. Intercalation compounds of graphite. Advances in Physics, 51(1), pp.1-186.

[18] Zhang, C., Ma, J., Han, F., Liu, H., Zhang, F., Fan, C., Liu, J. and Li, X., 2018. Strong anchoring effect of ferric chloride-graphite intercalation compounds ($FeCl_3$-GICs) with tailored epoxy groups for high-capacity and stable lithium storage. Journal of Materials Chemistry A, 6(37), pp.17982-17993.

[19] Postnikov, V.A., Zvarykina, A.V., Salyn, Y.V., Struchkov, Y.T. and Novikov, Y.N., 1977. Synthesis and structure of layer-type graphite compounds with ruthenium, palladium, and osmium chlorides. Journal of Structural Chemistry, 18(6), pp.819-822.

[20] Nayak, C., Simon, S.H., Stern, A., Freedman, M. and Sarma, S.D., 2008. Non-Abelian anyons and topological quantum computation. Reviews of Modern Physics, 80(3), p.1083.

[21] Kitaev, A.Y., 2003. Fault-tolerant quantum computation by anyons. Annals of Physics, 303(1), pp.2-30.

[22] Balents, L., 2010. Spin liquids in frustrated magnets. Nature, 464(7286), pp.199-208.

[23] Kawasaki, S., Takahashi, R., Akagi, K., Yoshinobu, J., Komori, F., Horiba, K., Kumigashira, H., Iwashina, K., Kudo, A. and Lippmaa, M., 2014. Electronic structure

and photoelectrochemical properties of an Ir-doped $SrTiO_3$ photocatalyst. The Journal of Physical Chemistry C, 118(35), pp.20222-20228.

[24] Takayama, T., Kato, A., Dinnebier, R., Nuss, J., Kono, H., Veiga, L.S.I., Fabbris, G., Haskel, D. and Takagi, H., 2015. Hyperhoneycomb Iridate β− Li_2IrO_3 as a Platform for Kitaev Magnetism. Physical Review Letters, 114(7), p.077202.

[25] Sandineni, P., Yaghoobnejad Asl, H., Gerasimchuk, N., Ghosh, K. and Choudhury, A., 2019. Soft chemical routes to electrochemically active iron phosphates. Inorganic Chemistry, 58(7), pp.4117-4133.

[26] Uppuluri, R., Gupta, A.S., Rosas, A.S. and Mallouk, T.E., 2018. Soft chemistry of ion-exchangeable layered metal oxides. Chemical Society Reviews, 47(7), pp.2401-2430.

[27] Winter, S.M., Tsirlin, A.A., Daghofer, M., van den Brink, J., Singh, Y., Gegenwart, P. and Valenti, R., 2017. Models and materials for generalized Kitaev magnetism. Journal of Physics: Condensed Matter, 29(49), p.493002.

[28] Gils, C., Trebst, S., Kitaev, A., Ludwig, A.W., Troyer, M. and Wang, Z., 2009. Topology-driven quantum phase transitions in time-reversal-invariant anyonic quantum liquids. Nature Physics, 5(11), pp.834-839.

[29] Banerjee, A., Yan, J., Knolle, J., Bridges, C.A., Stone, M.B., Lumsden, M.D., Mandrus, D.G., Tennant, D.A., Moessner, R. and Nagler, S.E., 2017. Neutron scattering in the proximate quantum spin liquid α-RuCl3. Science, 356(6342), pp.1055-1059.

[30] Banerjee, A., Bridges, C.A., Yan, J.Q., Aczel, A.A., Li, L., Stone, M.B., Granroth, G.E., Lumsden, M.D., Yiu, Y., Knolle, J. and Bhattacharjee, S., 2016. Proximate Kitaev quantum spin liquid behaviour in a honeycomb magnet. Nature Materials, 15(7), pp.733-740.

[31] Todorova, V., Leineweber, A., Kienle, L., Duppel, V. and Jansen, M., 2011. On $AgRhO_2$, and the new quaternary delafossites $AgLi_{1/3}M_{2/3}O_2$, syntheses and analyses of real structures. Journal of Solid State Chemistry, 184(5), pp.1112-1119.

[32] Kimber, S.A., Ling, C.D., Morris, D.J.P., Chemseddine, A., Henry, P.F. and Argyriou, D.N., 2010. Interlayer tuning of electronic and magnetic properties in honeycomb ordered $Ag_3LiRu_2O_6$. Journal of Materials Chemistry, 20(37), pp.8021-8025.

[33] Rau, J.G., Lee, E.K.H. and Kee, H.Y., 2014. Generic spin model for the honeycomb iridates beyond the Kitaev limit. Physical Review Letters, 112(7), p.077204.

[34] Khuntia, P., Manni, S., Foronda, F.R., Lancaster, T., Blundell, S.J., Gegenwart, P. and Baenitz, M., 2017. Local magnetism and spin dynamics of the frustrated honeycomb rhodate Li_2RhO_3. Physical Review B, 96(9), p.094432.

[35] Rüdorff, W., 1959. Graphite intercalation compounds. In Advances in Inorganic Chemistry and Radiochemistry (Vol. 1, pp. 223-266).

[36] Wang, F., Yi, J., Wang, Y., Wang, C., Wang, J. and Xia, Y., 2014. Graphite intercalation compounds (GICs): a new type of promising anode material for lithium-ion batteries. Advanced Energy Materials, 4(2), p.1300600.

[37] Noel, M. and Santhanam, R., 1998. Electrochemistry of graphite intercalation compounds. Journal of Power Sources, 72(1), pp.53-65.

[38] Flandrois, S., Masson, J.M., Rouillon, J.C., Gaultier, J. and Hauw, C., 1981. Intercalation compounds of graphite with nickel chloride: synthesis, structure, and mechanism of intercalation. Synthetic Metals, 3(1-2), pp.1-13.

[39] Tzeng, S.S., Wang, P.L. and Ko, T.H., 2001. Effects of processing parameters on the structure and amount of intercalation of copper chloride-graphite intercalation compounds. Journal of Materials Science, 36(2), pp.497-501.

[40] Lévy, F.A. ed., 2012. Intercalated layered materials (Vol. 6). Springer Science & Business Media.

[41] Flandrois, S., Amiell, J., Agricole, B., Stumpp, E., Ehrhardt, C. and Schubert, P., 1989. Magnetic properties of first-stage nickel chloride graphite intercalation compounds. Synthetic Metals, 34(1-3), pp.531-536.

[42] Hui, R., Kang, F.Y., Jiao, Q.J. and Shen, W.C., 2009. Synthesis criterion for a metal chloride-graphite intercalation compound by a molten salt method. New Carbon Materials, 24(1), pp.18-22.

[43] Flandrois, S., Hewat, A.W., Hauw, C. and Bragg, R.H., 1983. Neutron diffraction and small-angle scattering studies of graphite-nickel chloride intercalation compounds. Synthetic Metals, 7(3-4), pp.305-312.

[44] Nobuhara, K., Nakayama, H., Nose, M., Nakanishi, S. and Iba, H., 2013. First-principles study of alkali metal-graphite intercalation compounds. Journal of Power Sources, 243, pp.585-587.

[45] Stumpp, E., 1977. The intercalation of metal chlorides and bromides into graphite. Materials Science and Engineering, 31, pp.53-59.

[46] Rao, C.N.R. and Biswas, K., 2015. Ceramic methods. Essentials of Inorganic Materials Synthesis, pp.17-21.

[47] Matsumoto, R. and Okabe, Y., 2016. Electrical conductivity and air stability of $FeCl_3$, $CuCl_2$, $MoCl_5$, and $SbCl_5$ graphite intercalation compounds prepared from flexible graphite sheets. Synthetic Metals, 212, pp.62-68.

[48] Cullity, B.D., 1956. Elements of X-ray Diffraction. Addison-Wesley Publishing.

[49] Akahama, Y. and Kawamura, H., 2006. Pressure calibration of diamond anvil Raman gauge to 310 GPa. Journal of Applied Physics, 100(4), p.043516.

[50] Dubrovinsky, L., Dubrovinskaia, N., Prakapenka, V.B. and Abakumov, A.M., 2012. Implementation of micro-ball nanodiamond anvils for high-pressure studies above 6 Mbar. Nature Communications, 3(1), pp.1-7.

[51] Nesládek, M., Meykens, K., Stals, L.M., Vaněček, M. and Rosa, J., 1996. Origin of characteristic subgap optical absorption in CVD diamond films. Physical Review B, 54(8), p.5552.

[52] Warren, B.E., 1941. X-ray diffraction in random layer lattices. Physical Review, 59(9), p.693.

[53] Rao, G.V. and Shafer, M.W., 1979. Intercalation in layered transition metal dichalcogenides. In Intercalated layered materials (pp. 99-199). Springer, Dordrecht.

VITA

Nan Huang was born in Huzhong, Heilongjiang, China. She received his B.E. in Material Science and Engineering at the East China University of Science and Technology in 2015. In her senior year. She came to the United States for graduate studies. She received her M.S. in Chemical Engineering at the University of Missouri, Columbia, in 2016 with the thesis" Growing ZnO Nanowires Through Electrochemical Deposition For Spintronic Application In Metal-Insulator-Metal Structure As The Tunnel Junction.

In 2016, Nan Huang started to pursue her Ph.D. in the Material Science and Engineering department at UT. She has worked on multiple projects, including design development and characterization of novel spin liquid material synthesized by soft chemistry, flux growth, and CVD. After graduation. She will join Qualcomm as a Sr CAD software development engineer.